

NASA TECHNICAL NOTE



NASA TN D-5638

NASA TN D-5638

**LOCAL FLOW FIELD AROUND A
PYLON-MOUNTED DUMMY RAMJET
ENGINE ON THE X-15-2 AIRPLANE
FOR MACH NUMBERS FROM 2.0 TO 6.7**

by Frank W. Burcham, Jr., and Jack Nugent

*Flight Research Center
Edwards, Calif.*

1. Report No. NASA TN D-5638	2. Government Accession No.		3. Recipient's Catalog No.	
4. Title and Subtitle LOCAL FLOW FIELD AROUND A PYLON-MOUNTED DUMMY RAMJET ENGINE ON THE X-15-2 AIRPLANE FOR MACH NUMBERS FROM 2.0 TO 6.7			5. Report Date February 1970	
			6. Performing Organization Code	
7. Author(s) Frank W. Burcham, Jr., and Jack Nugent			8. Performing Organization Report No. H-566	
9. Performing Organization Name and Address NASA Flight Research Center P. O. Box 273 Edwards, Calif. 93523			10. Work Unit No. 722-01-00-01-24	
			11. Contract or Grant No.	
12. Sponsoring Agency Name and Address National Aeronautics and Space Administration Washington, D. C. 20546			13. Type of Report and Period Covered Technical Note	
			14. Sponsoring Agency Code	
15. Supplementary Notes				
16. Abstract <p>The flow field around a pylon-mounted dummy ramjet engine on the X-15-2 airplane was surveyed at Mach numbers from 2.0 to 6.7 in preparation for flight tests of a hydrogen-burning hypersonic ramjet engine. Impact pressures, local Mach number, and flow angularity were determined and compared with wind-tunnel data and theoretical calculations.</p> <p>The wing, camera fairing, and side fairing of the X-15-2 generated shock waves which impinged on the dummy ramjet and pylon. However, a region free of significant shock-wave impingement on the ramjet inlet existed for flight at a free-stream angle of attack of 5° or less for free-stream Mach numbers from 3.0 to 8.0.</p> <p>In flight regions free of shock-wave impingement, impact pressure, local Mach number, and angle of attack generally showed good agreement with wind-tunnel data. Shock-wave locations determined from impact-pressure data and wind-tunnel schlieren photograph data showed good agreement.</p> <p>Strong flow-interference effects occurred at the pylon-fuselage intersection. The separated-flow region and the resulting separation shock wave remained within 10 inches (25.4 centimeters) of the fuselage surface in front of the pylon for all flight conditions. The extent of separated flow was sensitive to angle of attack and extremely sensitive to small deviations from 0° in angle of sideslip.</p>				
17. Key Words Suggested by Author(s) X-15-2 - Flow field - Ramjet - Hypersonic research engine			18. Distribution Statement Unclassified - Unlimited	
19. Security Classif. (of this report) Unclassified	20. Security Classif. (of this page) Unclassified	21. No. of Pages 55	22. Price \$3.00*	

*For sale by the Clearinghouse for Federal Scientific and Technical Information,
Springfield, Virginia 22151.

CONTENTS

INTRODUCTION	1
SYMBOLS	2
TEST AIRPLANE AND DUMMY RAMJET ENGINE	3
TESTS	4
INSTRUMENTATION	4
DATA REDUCTION AND ANALYSIS	5
Shock-Wave Identification	5
Ramjet Flow-Field Parameters	6
Pylon and Ramjet Surface Pressures	6
ACCURACY	7
Pressure Measurements	7
Free-Stream Parameters	7
Calculated Flow Parameters	8
PRESENTATION OF RESULTS	8
DISCUSSION	9
Pylon Flow Field	9
Middle section of pylon	9
Pylon—ramjet intersection	9
Pylon—fuselage intersection	10
Flow model	10
Effect of α_∞	10
Effect of β_∞	11
Separation and forebody effects	11
Pylon surface pressure	12
Ramjet Flow Field	12
Shock-wave impingement in the ramjet region	12
Impact-pressure ratio	13
Shock-wave strength	13
Local-flow angularity	14
Local Mach number	15
Ramjet surface pressures	16
CONCLUSIONS	16
REFERENCES	18
FIGURES	21

LOCAL FLOW FIELD AROUND A PYLON-MOUNTED DUMMY RAMJET ENGINE ON THE X-15-2 AIRPLANE FOR MACH NUMBERS FROM 2.0 TO 6.7

By Frank W. Burcham, Jr., and Jack Nugent
Flight Research Center

INTRODUCTION

The National Aeronautics and Space Administration is engaged in the Hypersonic Research Engine Program (ref. 1). An initial object of this program was to conduct ground-based and flight tests on a hydrogen-burning ramjet engine over the Mach number range from 3 to 8. It was originally planned that engine ground-based tests would be followed by flights with the engine attached to the X-15-2 research airplane. In preparation for these tests, the NASA Flight Research Center conducted a flight program on the X-15-2 airplane with a dummy ramjet engine attached. The dummy ramjet had no internal air-flow and approximated the external contours of the engine now under development.

The purpose of these flights was to determine the effect of the ramjet installation on the stability and control of the X-15-2, to evaluate an ablative thermal protection system, and to establish airplane performance as the X-15-2 speed envelope was extended. In addition, flight measurements of the local flow conditions on and near the dummy ramjet were desired for use in integrating the ramjet engine with the X-15-2.

Satisfactory design and operation of the hydrogen-burning ramjet engine requires knowledge of the absolute values and extent of nonuniformity of the flow-field parameters of the air entering the engine inlet. Flow-field parameters of interest are the ratio of local to free-stream impact pressure, local flow angle, and Mach number. Knowledge of these parameters helps to establish inlet and overall engine performance and to assess possible effects of the engine operation on nearby portions of the airplane. It is also important to know the magnitude and variation of impact and surface pressures on the support pylon and surface pressures on the dummy ramjet. Knowledge of these pressures permits an assessment of aerodynamic loads, interference effects, and heating rates.

This report provides flow-field measurements from three X-15-2 flights with the dummy ramjet engine and from two earlier X-15-2 flights with an instrumented ventral fin installed. Data are shown for Mach numbers from 2.0 to 6.7 and altitudes up to 102,000 feet (31,000 meters). Airplane angle of attack varied from -1° to 12° , and angle of sideslip ranged from -2° to 2° . Flight Reynolds numbers in the ramjet region were from 20 million to 50 million, based on the 40-foot (12.2-meter) distance from the airplane nose to the ramjet spike. Data are compared with flow-field results obtained from wind-tunnel tests (refs. 2 and 3), flight data from the basic X-15 airplane (ref. 4), and theoretical calculations (ref. 5).

SYMBOLS

The units used for the physical quantities in this report are given in U. S. Customary Units and parenthetically in the International System of Units (SI). Factors relating the two systems are presented in reference 6.

C_p	pressure coefficient, $\frac{p_l - p_\infty}{q_\infty}$
d	maximum diameter of X-15 fuselage, 56 in. (142.2 cm)
h	geometric altitude, ft (m)
M	Mach number
N_{Re}	Reynolds number
p	static pressure, lb/sq ft (kN/sq m)
p_i	impact pressure (total pressure behind normal shock), lb/sq ft (kN/sq m)
q	dynamic pressure, $0.7 M^2 p$, lb/sq ft (kN/sq m)
x	longitudinal distance from airplane nose, in. (cm)
z	vertical distance down from lower-fuselage surface, in. (cm)
α	angle of attack, deg
β	angle of sideslip, deg
δ_w	wedge half angle, deg

Subscripts:

1	condition upstream of local shock wave
2	condition downstream of local shock wave
l	local condition
P	reference impact pressure at pylon leading edge
R	reference impact pressure at ramjet spike tip
sep	separation
shock	separation shock wave
∞	free-stream condition

TEST AIRPLANE AND DUMMY RAMJET ENGINE

The X-15-2 is a rocket-powered research airplane designed for flight to Mach numbers approaching 8. The airplane was modified from the basic X-15 by adding a 29-inch (73.6-centimeter) midfuselage extension and providing for jettisonable external propellant tanks to increase the burning time of the rocket engine. Reference 7 provides dimensional details on the basic X-15 airplane.

Figures 1 and 2 show, respectively, an in-flight photograph and a three-view drawing of the X-15-2 with the dummy ramjet installed. Figure 3 shows the two test configurations used to obtain flow-field data. As shown in figure 3(a), an instrumented lower ventral fin was attached to the fixed ventral fin. Figure 3(b) shows the dummy ramjet attached to the modified fixed ventral fin (hereafter referred to as the ramjet pylon). The modification consisted of removing the forward part of the fin and replacing it with an unswept blunt leading edge. A scale drawing of the dummy ramjet and ramjet pylon is shown in figure 4.

The dummy ramjet was fabricated from a series of truncated cones as an approximation to the hypersonic research engine. It was about 7 feet (2.1 meters) long and 2 feet (0.6 meter) in diameter at the base. Two nose configurations were flown, as shown in the photographs of figures 5(a) and 5(b). The dark band on the side of the ramjet in figure 5(a) was painted for optical tracking purposes.

For two of the flights, the X-15-2 pylon and dummy ramjet were coated with a charring ablative heat shield (fig. 5(b)) for thermal protection at high Mach numbers. Flight experience with this ablative coating is discussed in reference 8.

The smooth cylindrical surface of the lower fuselage of the X-15-2 was interrupted by a removable camera fairing installed for a hypersonic photography experiment (fig. 2). Figure 6 shows a sketch and a photograph of the camera fairing, which is about 13 feet (4.0 meters) upstream of the pylon. The maximum protuberance of the fairing is 1.75 inches (4.45 centimeters).

TESTS

The X-15-2 was air-launched from a B-52 airplane at a free-stream Mach number of approximately 0.8 and an altitude of 45,000 feet (13,700 meters). The powered acceleration was followed by a deceleration lasting from 3 to 5 minutes. During the deceleration, the pilot performed longitudinal and lateral-directional maneuvers at quasi-steady-state Mach numbers. The following table summarizes the maximum Mach number and altitude conditions reached during the three flights with the dummy ramjet and the earlier flights with the instrumented lower ventral fin:

Flight	X-15 flight designation	Maximum M_∞	Maximum h_∞ , ft (m)	Test configuration
A	2-44-79	5.43	100,000 (30,500)	Ventral probe on lower ventral fin
B	2-50-89	6.33	102,000 (31,000)	Ventral probe on lower ventral fin
C	2-51-92	4.72	96,000 (29,300)	Dummy ramjet engine with 20° nose cone
D	2-52-96	4.94	91,000 (27,700)	Dummy ramjet engine with ablative coating and 20° nose cone
E	2-53-97	6.70	102,000 (31,000)	Dummy ramjet engine with ablative coating and 40°-cone probes

Figure 7 shows the Mach number and angle-of-attack coverage for the test flights. Above $M_\infty = 5.5$, the test angle-of-attack range was limited.

Most of the data in this report were acquired during quasi-steady-state flight conditions. However, unless disturbed by the pilot, the free-stream angle of sideslip oscillated over a small amplitude range about a mean value with a frequency of about 0.5 cycle per second.

INSTRUMENTATION

Surface static-pressure orifices were located on the right side of the dummy ramjet and pylon at the positions shown in figure 4. Some of these orifices are also shown in figure 5(b). All orifices were normal to the surface and flush with the metal skin. When the ablative coating was applied, an insert of a higher density ablative material was used at each orifice location to maintain a sharp-edged orifice at the outer surface of the coating. The sharp edges of some of the orifices deteriorated during flight as ablation occurred.

Figures 4, 5, and 8 show the impact-pressure probes installed on the pylon leading edge. The probes were designed to extend through the pylon standoff shock wave except near the ramjet, where the probes were shortened to measure pylon—ramjet interference effects. A static-pressure orifice on the fuselage surface adjacent to the pylon probes is also shown in figure 8.

A 20° nose cone (fig. 5(a)) was faired into the ramjet spike and flown on two flights. Pressure orifices located as shown in figure 9 recorded pressures later used to calculate local Mach number and flow angularity. For one flight, the nose cone was replaced by a rake on which two 40°-cone probes were mounted (ref. 9). Figure 5(b) shows the cone probes mounted on the ramjet spike, with the center cone on the ramjet centerline and the lower cone 8 inches (20.3 centimeters) below.

Most of the pressures were recorded on standard types of optical-mechanical recorders by using either absolute or differential cells. An absolute reference pressure was provided for all the differential cells. The pylon impact pressures and pylon and ramjet surface pressures were connected to a 24-cell recorder. The ramjet nose cone and the 40°-cone-probe pressures were recorded on airspeed/altitude recorders similar to the 24-cell recorder but with higher resolution. The nose-cone impact pressures were recorded on differential cells which were referenced to one of the cone static-pressure cells. Tubing lengths from the pressure port to the pressure cell varied from about 5 feet to 10 feet (1.5 meters to 3 meters).

For the two flights flown with the lower ventral fin instead of the ramjet, an impact-pressure probe (fig. 3(a)) was installed on the leading edge of the ventral. This probe used an unbonded strain-gage pressure transducer.

Free-stream impact pressure $p_{i\infty}$, angle of attack α_∞ , and angle of sideslip β_∞ were obtained from the ball-nose flow-direction sensor, described in reference 10. Free-stream Mach number M_∞ , altitude h_∞ , and static pressure p_∞ were determined from a combination of sources, as described in reference 11.

DATA REDUCTION AND ANALYSIS

Shock-Wave Identification

Impact pressures from the dummy-ramjet pylon, spike, cone probes, and ventral impact-pressure probe, and static pressures from the fuselage orifice were non-dimensionalized by dividing by the free-stream impact pressure $p_{i\infty}$. Pylon impact-pressure ratio was plotted against individual probe position. Fairing of the pressure profiles was aided by detailed inspection of the pressure-time traces. Abrupt changes in the latter traces occurred at many times during the flights and were interpreted as the passing of shock waves. These abrupt changes were shown as discontinuities in the pressure profiles. With this technique, shock-wave location between adjacent pylon impact-pressure probes was established.

In addition, the strength of the shock wave in terms of impact-pressure ratio across the shock wave $\frac{p_{i2}}{p_{i1}}$ was assessed by the size of the impact-pressure increment noted on the pressure traces. In some instances pylon impact pressures near the ramjet exceeded the pressure-cell ranges. These pressures are indicated by dashed lines extending to the limit of the plot scale.

Impact-pressure traces for the dummy ramjet spike tip, cone probes, and ventral probe also showed passing shock waves. Free-stream Mach number and angle of attack for these occurrences were compared with the free-stream Mach number and free-stream angle of attack for known positions of shock waves as determined from 0.02-scale-model X-15 wind-tunnel schlieren photographs such as those of figures 10(a) and 10(b) and from 0.0667-scale-model schlieren photographs such as those of reference 12. By means of these comparisons, it was possible to identify the wing-leading-edge and side-fairing shock waves and their variations with M_∞ and α_∞ . An additional shock wave identified from the flight data was found to originate at the camera fairing on the bottom of the fuselage (fig. 6). This fairing was not on the wind-tunnel models tested and therefore its shock wave is not seen in schlieren photographs.

Ramjet Flow-Field Parameters

Pressure data from the 20° nose cone and the 40°-cone probes were reduced by using a digital-computer program. The results presented in this report are local Mach number, impact-pressure ratio, and flow angularity. A wind-tunnel calibration of the 40°-cone probes (ref. 9) was available, but cone theory (ref. 13) was used for the 20° nose cone. Reference 9 provides an example of the procedure used to convert the pressures to flow-field parameters for the 40°-cone probes. A similar procedure was used for the 20° nose cone.

Because of the long lengths of tubing connecting the cone orifices to the pressure cells, there was a considerable pressure lag during transient flight conditions, particularly in the static-pressure measurements. Consequently, the data were considered valid only during quasi-steady-state flight conditions.

Data from the 20° nose cone were considered questionable at local angles of attack in excess of about 3° and are not presented. It was believed that flow separation existed on the leeward side of the cone, as discussed in reference 14.

An additional method of determining local angle of attack from wind-tunnel data was used. The shock-wave angles from the dummy ramjet spike were measured on schlieren photographs such as those of figures 10(a) and 10(b). By using the known cone angle and an approximate local Mach number, the local flow angle α_l was calculated.

Pylon and Ramjet Surface Pressures

Surface static pressure on the pylon and ramjet were converted to pressure coefficients, that is, $C_p = \frac{p_l - p_\infty}{q_\infty}$. These coefficients were referenced to a pressure coefficient obtained from a local impact-pressure measurement $C_{pP} = \frac{p_{iP} - p_\infty}{q_\infty}$ or $C_{pR} = \frac{p_{iR} - p_\infty}{q_\infty}$. For the pylon, the reference p_{iP} was the impact-pressure probe immediately ahead of the row of static pressures. (See figs. 4 and 8.) For the ramjet-body static pressures, either the 20° nose cone or the 40°-center-cone probe impact pressure p_{iR} was used as the reference.

Flow-field data from wind-tunnel tests (refs. 2 and 3), a previous flight study (ref. 4), and a theoretical study (ref. 5) were obtained for the basic X-15 airplane, which is 29 inches (73.6 centimeters) shorter than the X-15-2. To compare these data with the present test results, the nose of the airplane was used as a common dimensional reference. The survey stations for the data discussed herein are shown in figure 11. The reference survey stations were all located upstream of the dummy ramjet and pylon.

ACCURACY

Pressure Measurements

The instrument error of the pressures recorded on the 24-cell recorder was 1 percent of full scale; for the airspeed/altitude recorders the error was 0.25 percent of full scale (ref. 15). Because the cells were generally measuring less than full-scale pressures, the full-scale errors resulted in the increased errors shown in the following table for average flight conditions:

Measurement	Cell range	Percent error, full scale	Percent error, average flight condition
Ramjet nose-cone impact pressure or 40° -cone-probe impact pressure	0 to 4000 psfd (0 to 191 kN/m ²)	0.25	1.0
Ventral-probe impact pressure	0 to 2160 psfa (0 to 103 kN/m ²)	1.0	2.0
Ramjet nose-cone static pressure and 40° -cone-probe static pressure	0 to 2000 psfa (0 to 96 kN/m ²)	0.25	1.5
Pylon impact pressure	0 to 2000 psfa (0 to 96 kN/m ²)	1.0	1.0
Pylon-surface static pressure	±650 psfd (±31 kN/m ²)	1.0	4.0
Ramjet-body static pressure	±650 psfd (±31 kN/m ²)	1.0	5.0
Fuselage-surface static pressure	±650 psfd (±31 kN/m ²)	1.0	3.0

Free-Stream Parameters

The errors in the free-stream parameters (refs. 10 and 11) are shown below:

Parameter	Estimated maximum error
M_{∞}	±0.06
α_{∞}	±0.25°
β_{∞}	±0.25°*
$p_{i_{\infty}}$	±1.0 percent
p_{∞}	$\left\{ \begin{array}{l} \pm 3 \text{ percent at } M_{\infty} = 6.0 \\ \pm 2 \text{ percent at } M_{\infty} = 4.65 \\ \pm 1 \text{ percent at } M_{\infty} = 3.0 \end{array} \right.$

*Although the absolute error in β_{∞} is ±0.25°, the incremental difference in β_{∞} at consecutive times is believed to be accurate to within ±0.1°.

Calculated Flow Parameters

Errors in the calculated flow parameters were determined by using the pressure-measurement errors and cone-calibration uncertainties (ref. 9). By using the methods of reference 16, the following estimated errors were obtained:

M_∞	Estimated error in -		
	M_l	α_l , deg	β_l , deg
3	± 0.05	± 0.5	± 0.5
4	± 0.07	± 0.5	± 0.5
4.65	± 0.16	± 0.5	± 0.5
6.5	± 0.28	± 0.5	± 0.5

Local Mach number and flow angles were calculated from the 20°-nose-cone pressure data by using cone theory (ref. 13). However, good agreement between the 20°-cone data and the calibrated 40°-cone data indicates that the theory applied to the 20° cone gave reasonably accurate results, at least for local angles of attack less than 3°.

Pressure coefficients calculated for the pylon and ramjet surface pressures are accurate to within about 5 percent of their absolute values, except when the values approach zero. For a pressure coefficient of 0.10, the error is 0.005, whereas for a pressure coefficient of 0.02, the error is ± 0.003 .

PRESENTATION OF RESULTS

Measurements made in the dummy-ramjet and pylon flow fields are presented as follows:

Pylon flow field —	Figure
Pylon impact-pressure data	12, 13, 14
Spike-tip shock-wave position	15
Pylon—fuselage interference flow	16, 17
Pylon surface static pressure	18
Ramjet flow field —	
Shock-wave positions in the ramjet region	19
Impact-pressure ratios in the ramjet region	20, 21
Shock-wave strength	22
Shock-free corridor	23
Local flow angularity	24, 25
Local Mach number	26, 27, 28
Ramjet surface static pressures	29

DISCUSSION

Pylon Flow Field

Figure 12 presents impact pressure on the pylon leading edge as a function of free-stream Mach number and angle of attack and probe position for $\beta_\infty = 0.5^\circ$. Figure 13 shows the effect of angle of sideslip on pylon impact pressure at $M_\infty = 3.0$ and $\alpha_\infty = 5^\circ$. Discontinuities shown in the data fairings in both figures are due to shock waves impinging on the pylon. The large changes in impact-pressure ratio evident in these figures are conveniently analyzed by isolating three local probe regions on the pylon as follows:

1. Probes in the middle section of the pylon (usually 10 to 12 inches (25.4 to 30.5 centimeters) below the fuselage), relatively free of ramjet and fuselage effects.
2. Pylon probes near the ramjet which are affected by flow at the pylon-ramjet intersection ($z \approx 13$ to 16 inches (33 to 41 centimeters)).
3. Pylon probes near the fuselage which are affected by flow at the pylon—fuselage intersection ($z \approx 0$ to 9 inches (0 to 23 centimeters)).

Middle section of pylon.— Under most conditions, the middle-ylon impact-pressure ratios remain relatively free of pylon—ramjet and pylon—fuselage flow interactions. Figure 12 shows that these pressure ratios increase with increasing angle of attack, whereas figure 13 illustrates that these pressure ratios were independent of angle of sideslip.

Impact-pressure ratios for a probe 10 inches (25.4 centimeters) below the fuselage surface are shown in figure 14 as a function of M_∞ and α_∞ . Good agreement with wind-tunnel data is shown at $\alpha_\infty = 0^\circ$ and 5° . The wing-leading-edge shock wave impinges on the probe at about $M_\infty = 5.4$ and $\alpha_\infty = 8^\circ$, causing the discontinuity in the data fairing. This wing shock wave can be seen impinging on the pylon in the wind-tunnel schlieren photograph of figure 10(b) and is observed in the pylon-rake impact-pressure data in figure 12(d). Wind-tunnel data were obtained upstream of the pylon and therefore do not show the wing shock wave.

Pylon—ramjet intersection.— Figures 12 and 13 show that the impact-pressure ratios obtained from the pylon probes near the dummy ramjet are higher than those in the middle of the pylon. These probes are within the conical shock wave generated by the ramjet spike tip. At Mach numbers of 4.0 and lower, the secondary shock wave generated by the flare in the ramjet spike also affects the probes closest to the ramjet. This spike-flare shock wave generates large impact-pressure ratios, as seen in figures 12(a) and 12(b). At higher Mach numbers this shock wave was located between the ramjet and the impact probe closest to the ramjet.

The position of the spike-tip shock wave on the pylon was a function of Mach number and angle of attack. Figure 15 shows this shock-wave position as determined from pylon-probe pressure data. At high Mach numbers, this shock wave is close to the ramjet, regardless of angle of attack. The prolonged impingement of both the spike-tip and

spike-flare shock waves on the pylon contributed to severe structural heating on flight E. This is discussed in detail in references 17 and 18.

Pylon—fuselage intersection.— Probes closest to the fuselage often showed about the same pressure ratio as that at the fuselage static-pressure orifice, which suggests that the flow was separated. In addition, impact probes farther from the fuselage showed abrupt pressure changes, indicating that a shock wave existed. Schlieren photographs in reference 12 showed a complex flow region ahead of the pylon. A flow model, based on wind-tunnel tests and the present flight data, helps to account for these observed flow effects.

Flow model: Several wind-tunnel studies (refs. 19 to 23) have tested a flow configuration consisting of a circular cylinder normal to a flat plate. This configuration resembles the X-15-2 pylon—fuselage intersection. A flow model derived from these studies and the flight results is shown in figure 16. The flow model shows a supersonic flow and a turbulent boundary layer in front of the pylon. The boundary layer separates ahead of the pylon and generates a separation shock wave which intersects the pylon standoff shock wave. Physical parameters defined in the flow model are as follows:

z_{sep}	postulated thickness of the separated region at the impact-pressure rake
z_{shock}	distance from the fuselage to the separation shock wave
$\frac{P_{i2}}{P_{i1}}$	impact-pressure ratio across the separation shock wave

The wind-tunnel tests had a uniform approach flow, no angularity effect, and a well-defined turbulent flat-plate boundary layer. For the X-15 flight data, the approach flow was nonuniform, with three-dimensional effects due to the cylindrical fuselage. The boundary layer could not be defined easily because of protuberances such as the camera fairing directly upstream of the pylon.

Figure 17 compares the impact-pressure data on a cylinder from reference 19 with the X-15 data at a similar Mach number. Reasonable agreement in shock-wave location and in impact pressure in the region outside the interference effect is shown. The impact pressures in the interference region are somewhat lower for the flight data, possibly because of different pressure-measurement locations. Wind-tunnel impact pressures were measured at the cylinder surface, whereas in flight the impact-pressure probes extended more than 3 inches (7.6 centimeters) ahead of the pylon. In addition, the three-dimensionality of the flow in flight would reduce the impact pressures. The reasonable agreement between wind-tunnel and flight data indicates that the flow model is valid for analysis of flight data.

Effect of α_{∞} : In order to analyze the data for the effects of α_{∞} alone through the Mach number range, a nominal angle of sideslip had to be selected. As discussed in the TESTS section, β_{∞} varied continuously over a small range during the flights. It was observed that as β_{∞} deviated from 0° , in either a positive or negative direction, the impact-pressure probes near the fuselage showed steadily increasing pressures until β_{∞}

reached approximately $\pm 0.5^\circ$. Further deviation in β_∞ beyond $\pm 0.5^\circ$ resulted in only small changes in the impact pressures. As a result, most of the impact-pressure data obtained were equivalent to a nominal value of $\beta_\infty = \pm 0.5^\circ$. This value was therefore chosen for analysis.

Figure 12 indicates that increasing the level of α_∞ increases the impact-pressure ratio for all Mach numbers. In figures 12(a), 12(b), and 12(c), the thickness of the separated region z_{sep} and the distance from the fuselage to the separation shock wave z_{shock} decrease with increasing angle of attack at a given Mach number. At $\alpha_\infty = 5^\circ$, z_{shock} moves down the pylon as M_∞ increases from 3.0 to 4.65. The data also show that for $\alpha_\infty \approx 5^\circ$ the strength of the separation shock wave $\frac{p_{i2}}{p_{i1}}$ decreases with increasing Mach number. At $M_\infty = 6.5$ (fig. 12(d)) there is no evidence of the separation shock wave, but the wing-leading-edge shock wave is identifiable.

Effect of β_∞ : The data of figure 13 were analyzed for the effects of β_∞ with M_∞ and α_∞ fixed. Increasing β_∞ from about 0° to about 0.5° steadily decreases the thickness of the separated region z_{sep} and the distance from the fuselage to the separation shock wave z_{shock} . Increasing β_∞ also sharply increases the pressure-ratio level for a particular probe near the fuselage but does not affect the strength of the separation shock wave $\frac{p_{i2}}{p_{i1}}$. Similar strong effects of β_∞ were noted at other Mach numbers.

Separation and forebody effects: Flow near the pylon—fuselage intersection is dominated by the separation region and the separation shock wave. Pylon impact-pressure data show that the flow-interference effects at the intersection remained within 10 inches (25.4 centimeters) of the fuselage for all the flight conditions. The data of reference 17 show that severe interference heating caused by the pylon—fuselage interference flow extended about 1 inch (2.54 centimeters) upstream of the pylon. This heating caused complete erosion of the ablative coating on the fuselage and some permanent skin buckling.

The sensitivity of the separation region to α_∞ and β_∞ is believed to be due to the X-15-2 forebody effects on the fuselage boundary layer. Thus, at low angles of attack and $\beta_\infty = 0^\circ$, the forebody boundary layer immediately ahead of the pylon tends to be thick. Consequently, impact-pressure ratios near the fuselage surface are low. As β_∞ changes from 0° , forebody crossflow velocities are induced and reduce the boundary-layer thickness ahead of the pylon. As a result, the pylon impact pressures rise sharply as shown in figure 13, particularly for the third probe down from the fuselage. A similar reduction of the boundary-layer thickness due to crossflow around the fuselage occurs as angle of attack increases, as seen in figure 12.

Pylon surface pressure. — Pylon surface pressure-coefficient ratios are plotted in figure 18 for $M_\infty = 3.0, 4.65, \text{ and } 6.5$. Data were obtained for several values of α_∞ for the X-15-2 both with and without the ablative coating. Newtonian theory (ref. 24) was used to predict surface pressure-coefficient ratios for the pylon.

No effects of α_∞ or the ablative coating were evident from the flight data. The data near the leading edge of the pylon agree with Newtonian theory. An increase in pressure-coefficient ratio is noted between the fourth and fifth orifices from the reference probe. It is believed that shock waves originating at the leading edge of the landing skid (fig. 3) and the ramjet spike shock cause the increase. Surface pressure measurements on the unmodified ventral fin (ref. 25) also showed skid shock-wave effects.

Ramjet Flow Field

Shock-wave impingement in the ramjet region. — Figure 19 shows the combinations of M_∞ and α_∞ where shock waves from the wing, camera fairing, and fuselage side fairing impinged on four flight impact-pressure probes. Data from wind-tunnel schlieren photographs are also shown. Reynolds numbers for the schlieren photograph data ranged from 5 percent to 62 percent of the flight values.

In figure 19(a), the wing shock wave impinges on the ramjet spike tip at Mach numbers less than 4 for the angle-of-attack range shown. Figure 10(a) shows an example of this occurrence during wind-tunnel tests. The curve for the wing shock-wave impingement on the ventral probe has the same shape as for the spike tip but is shifted to higher Mach numbers because the ventral probe is farther downstream and closer to the fuselage than the spike tip (fig. 11). The curve for the wing shock impinging on the lowest pylon probe is shifted to still higher Mach numbers. Combinations of M_∞ and α_∞ above the curve cause the wing shock wave to impinge on the pylon (figs. 10(b) and 12(d)); for flight conditions below this curve, the wing shock is incident on the ramjet spike. Wind-tunnel schlieren photograph data show excellent agreement with the flight data for all three impact-probe locations.

Figure 19(b) shows the location of the camera-fairing shock wave as detected at the lower 40° cone, the spike tip, and the ventral probe. The trends shown are similar to those of the wing shock-wave data. The ablative coating slightly changed the location of the shock wave for the spike tip. The direction of the change is consistent with a decreased shock inclination due to the increased protuberance of the coated camera fairing.

In figure 19(c) above $M_\infty = 6.2$ for $\alpha_\infty = 6^\circ$ to 8° , the side-fairing shock wave impinged on the lower 40° -cone probe but did not reach the center cone. Good agreement with schlieren photograph data is again shown.

From figures 19(a) and 19(c), it is apparent that the Reynolds number differences between wind-tunnel and flight tests did not significantly affect shock-wave locations in the ramjet region.

Impact-pressure ratio.— The impact-pressure ratio $\frac{p_{iL}}{p_{i\infty}}$ is a flow-field parameter

of interest for ramjet performance and is shown for the ramjet spike tip and ventral impact-pressure probe in figures 20(a) and 20(b), respectively. Wind-tunnel data (ref. 2) and data obtained from theoretical calculations (ref. 5) are also shown. At Mach numbers between about 2.6 and camera-fairing shock passage, both figures show the gradual increase in impact-pressure ratio at the higher angles of attack due to the approaching camera-fairing shock wave. When the shock wave passes the spike tip or ventral probe, impact pressure drops sharply.

For Mach numbers above that for shock passage, impact pressure is strongly affected by angle of attack. Both figures show that at $M_\infty = 6.5$, a 1° increase in α_∞ increases the impact pressure by almost 10 percent for angles of attack greater than 5° . Spike-tip and ventral-probe data show good agreement with each other and with wind-tunnel data at $M_\infty = 6^\circ$. The theoretical values agree with wind-tunnel data at $\alpha_\infty = 0^\circ$, but predict lower impact pressures than either the wind-tunnel or flight data at higher angles of attack. Disagreement between wind-tunnel data, flight data, and theoretical values at $M_\infty = 4.0$ and 4.65 is attributed to the camera-fairing shock wave.

Figure 21 shows the effect of fuselage station at $\alpha_\infty = 2^\circ$ on impact-pressure ratios at the spike tip, ventral probe, middle pylon probe, and at an impact-pressure probe flown on the basic X-15 in a previous study (ref. 4). The ratio $\frac{z}{d}$ varies from 0.18 to 0.45, but the data of reference 2 show only small effects of $\frac{z}{d}$ on $\frac{p_{iL}}{p_{i\infty}}$ in the M_∞ and α_∞ range covered. At $M_\infty = 2.0$ and 6.0 , impact-pressure ratio increases with increasing $\frac{x}{d}$, with the increase being much larger at $M_\infty = 2.0$.

Shock-wave strength.— A direct measure of shock-wave strength is the ratio $\frac{p_{i2}}{p_{i1}}$. Figure 22 shows $\frac{p_{i2}}{p_{i1}}$ as a function of M_∞ and α_∞ for the wing-leading-edge, camera-fairing, and fuselage side-fairing shock waves. As shown, the strength of these shock waves increases with increasing M_∞ and α_∞ . At a constant α_∞ , the shock-wave strength appears to increase almost linearly with increasing M_∞ .

The wing-leading-edge shock wave is very weak when it crosses the spike tip at about $M_\infty = 3$, as shown in figure 20(a). However, when the wing shock impinges on the pylon at $M_\infty = 6.5$ and $\alpha_\infty = 8.4^\circ$ (figs. 22(a) and 12(d)), the impact-pressure ratio is much higher.

The strength of the camera-fairing shock wave, shown in figure 22(b), also increases with increasing M_∞ and α_∞ . The increase in shock-wave strength with Mach number is somewhat less than for the wing shock wave.

The side-fairing shock wave was detected only at Mach numbers of 6.2 and greater. In figure 22(c) the increase in shock-wave strength with Mach number for the side-fairing shock wave is greater than for the wing or camera-fairing shock waves.

On the basis of the shock-wave strength determined in figure 22 and the shock-wave locations shown in figure 19, it is possible to determine the flight conditions which minimize or eliminate shock-wave impingement on the inlet of the hypersonic research engine (HRE). Since the camera fairing would be removed for HRE testing, the camera-fairing shock wave need not be considered.

Figure 23 is a composite of figures 19 and 22, showing the strength and location of the wing and side-fairing shock waves on a plot of M_∞ versus α_∞ . A shock-free corridor exists above the wing shock-wave-impingement region and below the side-fairing shock-wave-impingement region. For Mach numbers below the corridor at the lower angles of attack, the wing shock wave is weak and probably would not affect the HRE inlet. The side-fairing shock wave is stronger than that of the wing and should be avoided. For angles of attack up to 5° , it appears that the HRE could be tested without significant shock-wave impingement over the desired Mach number range from 3.0 to 8.0.

Local flow angularity.— Local flow angles at the ramjet spike tip and 40° center cone are plotted against free-stream angle of attack for several test Mach numbers in figure 24. An increase in airplane angle of attack of about 4° increases the local angle of attack 1° at the lower Mach numbers. At a given free-stream angle of attack, the local angle of attack decreases with increasing Mach number. Local angles of attack are positive for zero free-stream angle of attack, but the curves suggest that at M_∞ greater than about 6.0, local angle of attack would become negative at $\alpha_\infty = 0^\circ$.

For a nominal 5° free-stream angle of attack, the local angle of attack was 3° , 2° , and $1\ 1/2^\circ$ at $M_\infty = 3.0$, 4.5, and 6.0, respectively. This result suggests that the HRE should be canted down approximately 2° from the X-15 fuselage centerline to minimize the range of local angle of attack over which the inlet must operate.

Limited flow-angle data were obtained at the lower 40° -cone probe in flight E. When compared with the local angle of attack obtained at the center cone, the two sets of data were nearly equal at $M_\infty = 4.0$, but the lower cone values were about 1° higher at $M_\infty = 6.0$.

Flight-determined local angles of attack at the ramjet spike tip are compared with local angles of attack from theoretical calculations and wind-tunnel tests at $M_\infty = 4.0$ and 6.0 in figures 25(a) and 25(b), respectively. The theoretical data (ref. 5) were obtained for the flow under an ogive cylinder, neglecting protuberances such as wings, side fairings, and canopy. Disagreement between theoretical and flight data increases with increasing angle of attack for the two Mach numbers. It is believed that the wing and side fairing, which would tend to reduce flow angles, cause the disagreement. Wind-tunnel flow-angle data (ref. 2) show good agreement in level and trend with the flight data at $M_\infty = 4.0$. At $M_\infty = 6.0$, the agreement is only slightly less favorable. Comparison of the local angle of attack obtained in flight with that obtained from the wind-tunnel schlieren photographs yielded good agreement at both Mach numbers. This latter technique is easy to apply and, from the results, appears to be useful for flow-field studies.

Local angles of sideslip at the ramjet spike tip were obtained along with the local-angle-of-attack data. The angles of sideslip were within $\pm 1^\circ$ for all test conditions. The flow off the vertical plane of symmetry was not surveyed in flight; however, the data of references 2 and 3 show definite sideslip flow angles at these locations.

Local Mach number.— Local Mach number obtained from the 20° cone on flights C and D and the 40° -cone probes on flight E is plotted against free-stream Mach number in figures 26(a) and 26(b). Free-stream angle of attack and a reference line $M_L = M_\infty$ are also shown. Sketches of the relative position of the camera-fairing shock wave and appropriate spike-tip configuration appear where the shock wave influences the data. All data show that M_L was smaller than M_∞ .

With the 20° nose cone (fig. 26(a)) the approaching shock wave begins to reduce the rate of increase of M_L at about $M_\infty = 3.3$, as indicated by the slight slope decrease. The slope remains constant until $M_\infty = 4.7$, where the shock crosses the spike tip, and the local Mach number then increases rapidly by about 0.3. The angle of attack remained at approximately 0.5° during shock passage.

In figure 26(b) similar results are noted for the camera-fairing shock interacting with the two 40° -cone probes. For M_∞ below about 3.2 to 3.3, the shock wave lies below both cones, and the local Mach numbers are reasonably close. When the shock wave crosses the lower cone, M_L increases markedly, whereas M_L for the upper cone is not affected. Increasing M_∞ from about 3.4 to 4.6 steadily increases M_L for both cones. The increment in M_L between the two cones remains constant at about 0.25 to 0.30 until, at about $M_\infty = 4.6$, the shock crosses the upper cone. From $M_\infty = 4.6$ to 5.0, both cones lie under the shock wave, and the local Mach numbers once again agree closely. The small slope changes in M_L for the cones are associated with the small angle-of-attack changes.

The local Mach numbers at the ramjet spike tip from figures 26(a) and 26(b) are compared with corresponding data from wind-tunnel tests (ref. 2) and theoretical calculations (ref. 5) for comparable angles of attack in figure 27. At $M_\infty = 4.0$, M_L from the 40° -lower-cone probe shows good agreement with wind-tunnel data and theoretical values. As shown in figure 26(b), the camera-fairing shock wave lies between the cone probes at this Mach number. Consequently, the center cone or 20° nose cone shows a lower M_L than either theoretical or wind-tunnel data. At $M_\infty = 6.0$ and $\alpha_\infty \approx 4^\circ$ to 6° , M_L from both flight sources again shows good agreement with wind-tunnel data and theoretical values. The data of figure 23 indicate that the ramjet-spike tip was free from any incident shocks for these flight conditions.

The comparisons in figure 27 show that flight measurements of M_L for $M_\infty = 3.0$ to about $M_\infty = 6.5$ agree well with wind-tunnel data and reasonably well with theory, provided the camera-fairing shock wave lies behind the front portion of the spike. Good agreement would likely be obtained for all flight conditions if the camera fairing were removed. It appears that the theory of reference 5 is useful for predicting local Mach number although it does not account for such factors as the wings or side fairings of the X-15.

Performance estimates for hypersonic propulsion systems installed under vehicle fuselages or wings are often made by assuming a favorable interference compression field from these components (refs. 26 and 27). A measure of the favorable interference is the reduction in local Mach number from the free-stream value. For ease in calculation, it is assumed that the bottom of the vehicle fuselage or wing is a flat surface inclined to the free-stream flow vector at the airplane angle of attack. Oblique-shock theory (ref. 28) is then used to calculate the local Mach number or other parameters of interest.

Figure 28 is a plot of M_l at the ramjet spike tip versus M_∞ for angles of attack 0° , 5° , and 10° . The dashed lines show M_l obtained from oblique-shock-wave theory. The solid lines show M_l at the spike tip based on the present test data, assuming that the camera fairing were removed. Wind-tunnel measurements were used to extend the test data. The local Mach number for the spike tip increases uniformly with M_∞ for all angles of attack but indicates less compression than would be obtained for a two-dimensional flow field for $\alpha_\infty = 5^\circ$ and 10° . Slight compression is noted at $\alpha_\infty = 0^\circ$. At $\alpha_\infty = 5^\circ$, M_l is 2.85, 4.2, and 5.5 for $M_\infty = 3.0$, 4.5, and 6.0, respectively.

Ramjet surface pressures.—Surface pressures measured on the right side of the dummy ramjet at the six locations shown in figure 4 are presented in figure 29. Data were obtained at angles of attack from 0° to 10° and at $\beta_\infty \approx 0^\circ$. The data show little sensitivity to Mach number and angle of attack. Modified Newtonian theory was used to predict the surface pressures; the theoretical values were slightly lower than those measured in flight.

CONCLUSIONS

A flight survey of the local flow field around a pylon-mounted dummy ramjet engine on the X-15-2 airplane for Mach numbers from 2.0 to 6.7 yielded the following conclusions:

1. The wing, lower-fuselage camera fairing, and fuselage side fairing of the airplane generated shock waves which impinged on the dummy ramjet and pylon. However, a region free of significant shock-wave impingement on the ramjet inlet existed for flight at a free-stream angle of attack of 5° or less for free-stream Mach numbers from 3.0 to 8.0.
2. The local Mach number at the ramjet spike tip was always less than the free-stream Mach number and, at a constant Mach number, decreased with increasing free-stream angle of attack. For a nominal 5° angle of attack, the local Mach numbers were 2.85, 4.2, and 5.5 for free-stream Mach numbers of 3.0, 4.5, and 6.0, respectively.
3. Local angle of attack increased about 1° for a 4° increase in free-stream angle of attack over the Mach number range from 3.0 to 4.6. For a given free-stream angle of attack, increasing the free-stream Mach number decreased the local angle of attack. At a free-stream angle of attack of 5° , local angles of attack were 3° , 2° , and $1\frac{1}{2}^\circ$ at free-stream Mach numbers of 3.0, 4.5, and 6.0, respectively.

4. Impact pressures in the ramjet region became increasingly sensitive to angle of attack as Mach number increased. At a free-stream Mach number of 6.5, a 1° increase in free-stream angle of attack resulted in a 10-percent increase in impact pressure.

5. In flight regions free of shock-wave impingement, impact pressure, local Mach number, and angle of attack generally showed good agreement with wind-tunnel data. Shock-wave locations determined from impact-pressure data and wind-tunnel schlieren photographs also showed good agreement.

6. Strong shock waves generated by the ramjet spike at high Mach numbers impinged on the pylon, resulting in high impact pressures.

7. Strong flow-interference effects occurred at the pylon-fuselage intersection. The separated-flow region and the resulting separation shock wave ahead of the pylon remained within 10 inches (25.4 centimeters) of the fuselage surface for all flight conditions. The extent of separated flow was sensitive to angle of attack and extremely sensitive to small deviations from 0° in angle of sideslip.

Flight Research Center
National Aeronautics and Space Administration
Edwards, Calif., October 9, 1969

REFERENCES

1. Rubert, Kennedy F. : Hypersonic Air-Breathing Propulsion-System Testing on the X-15. Progress of the X-15 Research Airplane Program. NASA SP-90, 1965, pp. 127-132.
2. Montoya, Earl J. ; and Palitz, Murray: Wind-Tunnel Investigation of the Flow Field Beneath the Fuselage of the X-15 Airplane at Mach Numbers From 4 to 8. NASA TM X-1469, 1967.
3. Rippey, J. : Flow-Field Investigation of a 0.0667-Scale Model of the X-15 Research Vehicle at Mach 4, 6, and 8. AEDC-TDR-64-201, Arnold Eng. Dev. Center, Oct. 1964.
4. McLain, L. J. ; and Palitz, Murray: Flow-Field Investigations on the X-15 Airplane and Model Up to Hypersonic Speeds. NASA TN D-4813, 1968.
5. Gallo, William F. ; and Rakich, John V. : Investigation of Methods for Predicting Flow in the Shock Layer Over Bodies at Small Angles of Attack. NASA TN D-3946, 1967.
6. Mechtly, E. A. : The International System of Units - Physical Constants and Conversion Factors. NASA SP-7012, 1964.
7. Saltzman, Edwin J. ; and Garringer, Darwin J. : Summary of Full-Scale Lift and Drag Characteristics of the X-15 Airplane. NASA TN D-3343, 1966.
8. Cary, John P. : Experience With a Charring-Ablator Heat Shield on the X-15-2 Airplane to Mach 6.7. NASA TM X-1745, 1969.
9. Burcham, Frank W. , Jr. : Wind-Tunnel Calibration of a 40° Conical Pressure Probe at Mach Numbers From 3.5 to 7.4. NASA TN D-4678, 1968.
10. Wolowicz, Chester H. ; and Gossett, Terrence D. : Operational and Performance Characteristics of the X-15 Spherical, Hypersonic Flow-Direction Sensor. NASA TN D-3070, 1965.
11. Webb, Lannie D. : Characteristics and Use of X-15 Air-Data Sensors. NASA TN D-4597, 1968.
12. Graves, Ernald B. : Effect of Hypersonic Research Engine Installation on Aerodynamic Characteristics of 0.0667-Scale Model of X-15A-2 Airplane at Mach Numbers From 1.75 to 4.63. NASA TM X-1840, 1969.
13. Babenko, K. I. ; et al. : Three-Dimensional Flow of Ideal Gas Past Smooth Bodies. NASA TT F-380, "Science" Publishing House (Moscow), 1964. (Available from CFSTI, Springfield, Va.)
14. Ray, A. D. : Mach Number 3 to 8 Calibrations of a 30-Deg Conical Probe. AEDC-TR-66-168, Arnold Eng. Dev. Center, Sept. 1966.

15. Zalovcik, John A. : A Radar Method of Calibrating Airspeed Installations on Airplanes in Maneuvers at High Altitudes and at Transonic and Supersonic Speeds. NACA Rep. 985, 1949.
16. Barry, B. Austin: Engineering Measurements. John Wiley & Sons, Inc. , 1964.
17. Watts, Joe D. : Flight Experience With Shock Impingement and Interference Heating on the X-15-2 Research Airplane. NASA TM X-1669, 1968.
18. Edney, Barry: Anomalous Heat Transfer and Pressure Distributions on Blunt Bodies at Hypersonic Speeds in the Presence of an Impinging Shock. Rep. 115, The Aeron. Res. Inst. of Sweden, Feb. 1968.
19. Westkaemper, John Conrad: The Drag of Cylinders All or Partially Immersed in a Turbulent, Supersonic Boundary Layer. DRL-549, Def. Res. Lab., Univ. of Texas, Mar. 1, 1967. (Available from DDC as AD 813886.)
20. Miller, William H. : Pressure Distributions on Single and Tandem Cylinders Mounted on a Flat Plate in Mach Number 5.0 Flow. DRL-538, Def. Res. Lab., Univ. of Texas, June 1, 1966.
21. Sykes, D. M. : The supersonic and low-speed flows past circular cylinders of finite length supported at one end. J. Fluid Mech., vol. 12, part 3, Mar. 1962, pp. 367-387.
22. Price, Earl A. ; Howard, Paul W. ; and Stallings, Robert L., Jr. : Heat-Transfer Measurements on a Flat Plate and Attached Fins at Mach Numbers of 3.51 and 4.44. NASA TN D-2340, 1964.
23. Burbank, Paige B. ; Newlander, Robert A. ; and Collins, Ida K. : Heat-Transfer and Pressure Measurements on a Flat-Plate Surface and Heat-Transfer Measurements on Attached Protuberances in a Supersonic Turbulent Boundary Layer at Mach Numbers of 2.65, 3.51, and 4.44. NASA TN D-1372, 1962.
24. Ehret, Dorris M. : Accuracy of Approximate Methods for Predicting Pressures on Pointed Nonlifting Bodies of Revolution in Supersonic Flow. NACA TN 2764, 1952.
25. Pyle, Jon S. : Flight Pressure Distributions on the Vertical Stabilizers and Speed Brakes of the X-15 Airplane at Mach Numbers From 1 to 6. NASA TN D-3048, 1965.
26. Kirkham, Frank S. ; Cubbage, James M., Jr. ; Vahl, Walter A. ; and Small, William J. : Studies of Airframe-Propulsion-System Integration for Mach 6 Cruise Vehicles. Conference on Hypersonic Aircraft Technology, NASA SP-148, 1967, pp. 115-135.
27. Fetterman, David E. ; McLellan, Charles H. ; Jackson, L. Robert; Henry, Beverly Z., Jr. ; and Henry, John R. : A Review of Hypersonic Cruise Vehicles. Conference on Aircraft Aerodynamics, NASA SP-124, 1966, pp. 253-564.

28. Ames Research Staff: Equations, Tables, and Charts for Compressible Flow.
NACA Rep. 1135, 1953. (Supersedes NACA TN 1428.)

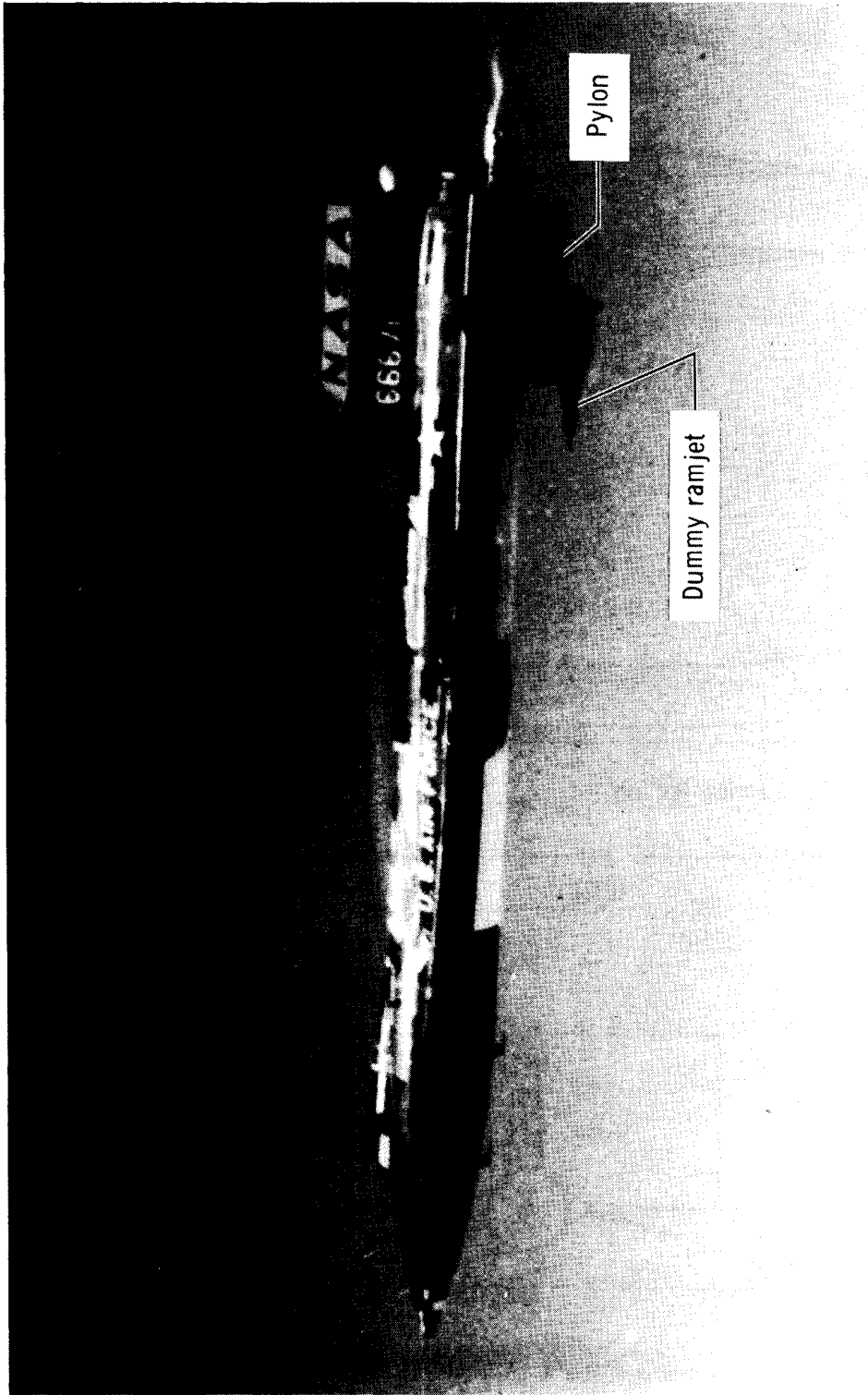


Figure 1. -- Photograph of the X-15-2 with the dummy ramjet installed.

E-16928

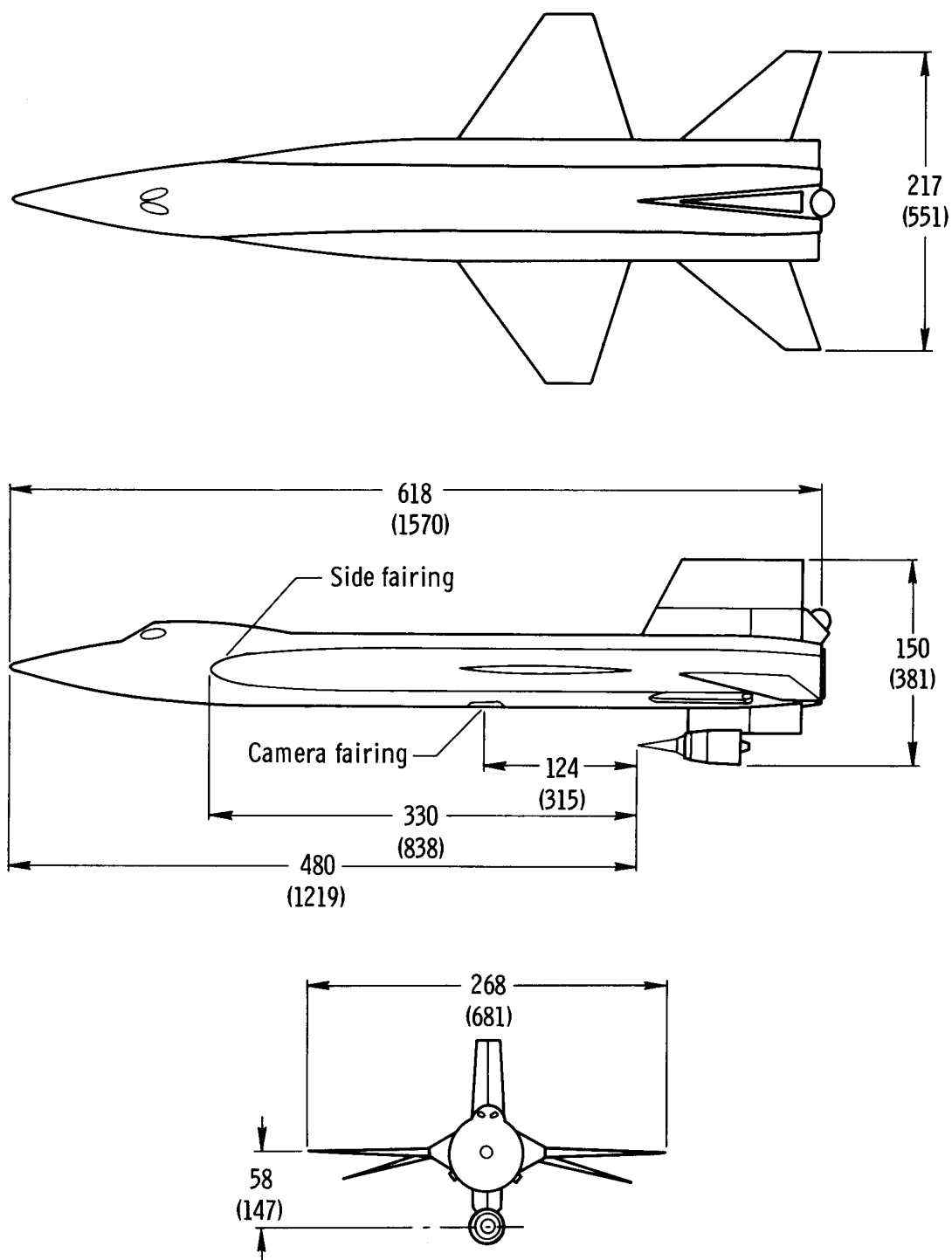
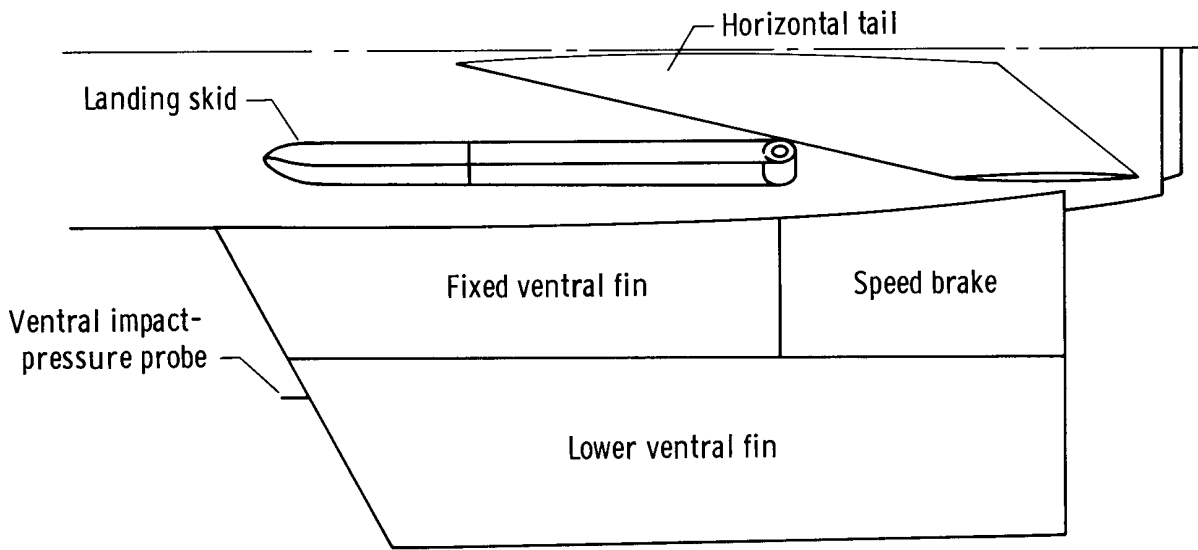
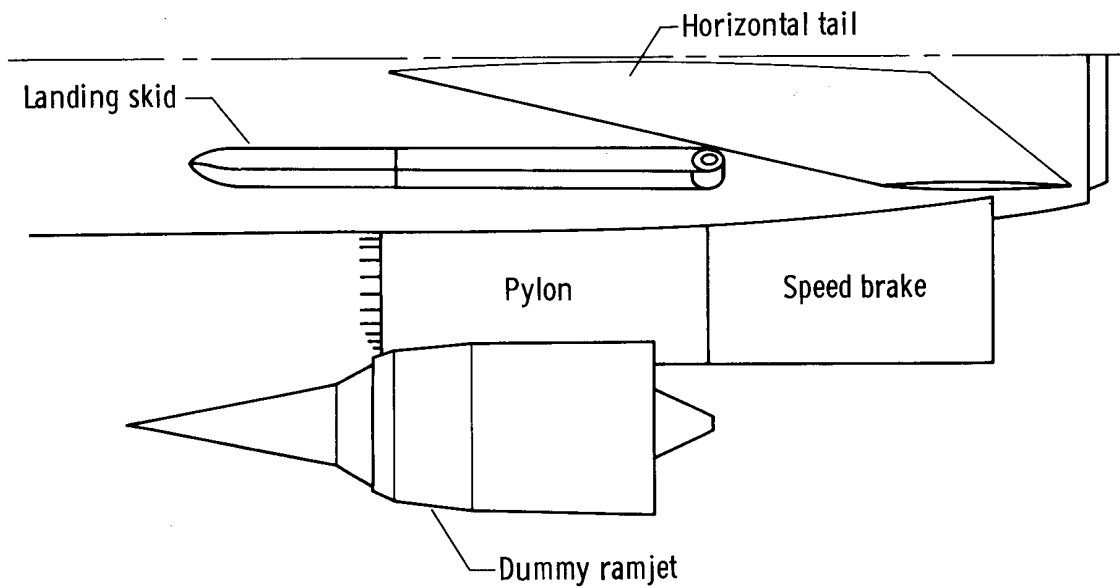


Figure 2.— Three-view drawing of the X-15-2 with the dummy ramjet installed.
All dimensions in inches (centimeters).



(a) Before modification, with lower ventral fin installed.



(b) After modification, with the dummy ramjet installed.

Figure 3.— Test configurations for local-flow-field tests.

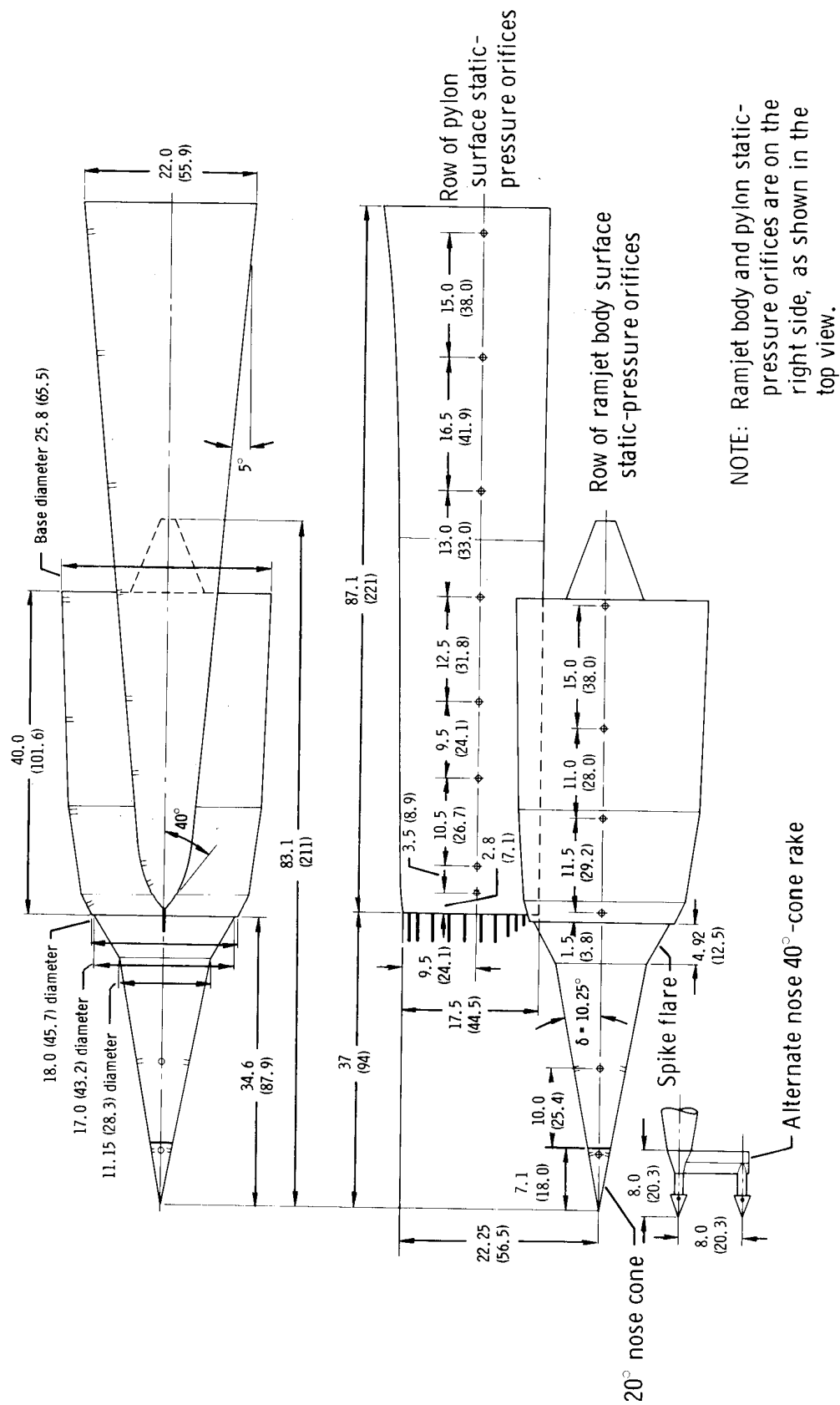
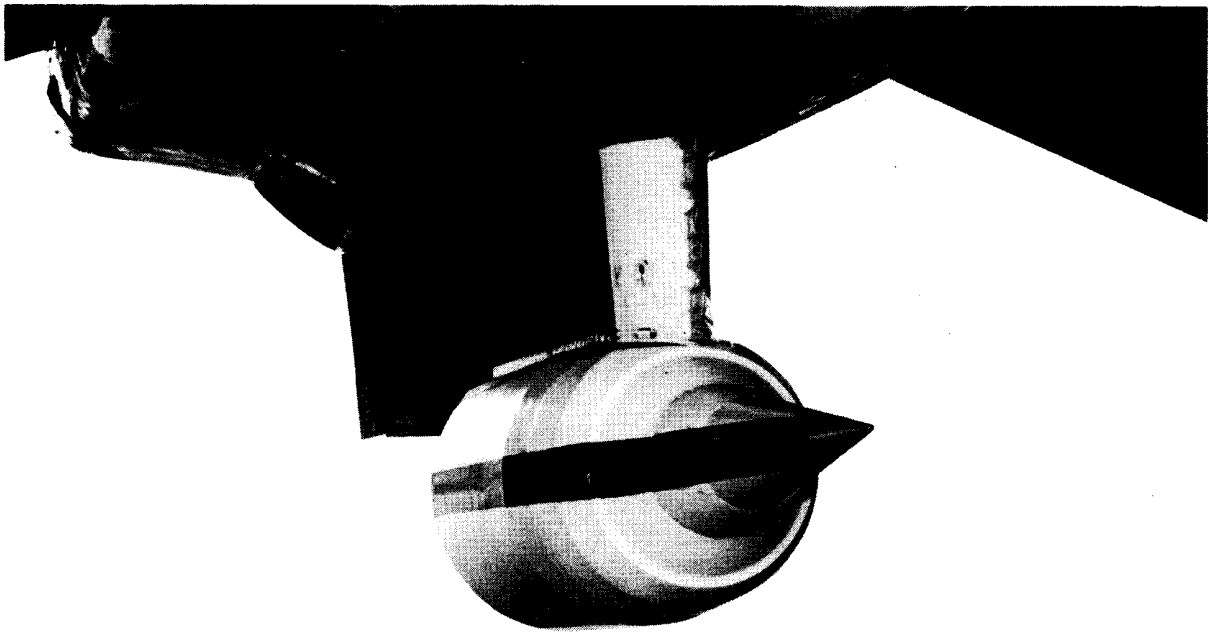
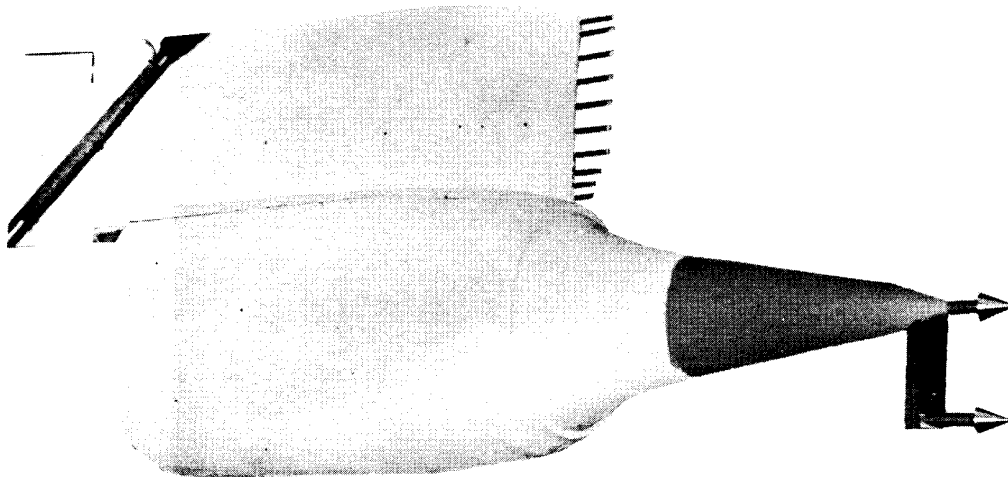


Figure 4. - Details of dummy ramjet and pylon, and locations of pressure-measuring instrumentation. All dimensions in inches (centimeters).



(a) Dummy ramjet with the 20° nose cone.

E-16692



(b) Dummy ramjet with the 40°-cone probe rake and ablative coating.

E-17493

Figure 5. — Photographs of the dummy ramjet and pylon showing the two nose configurations tested.

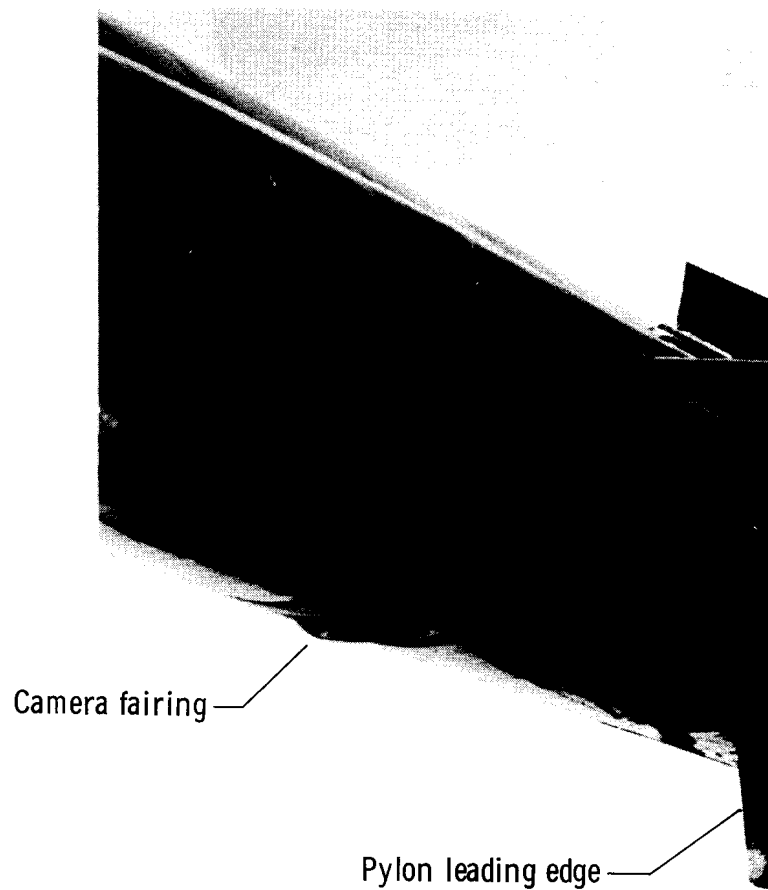
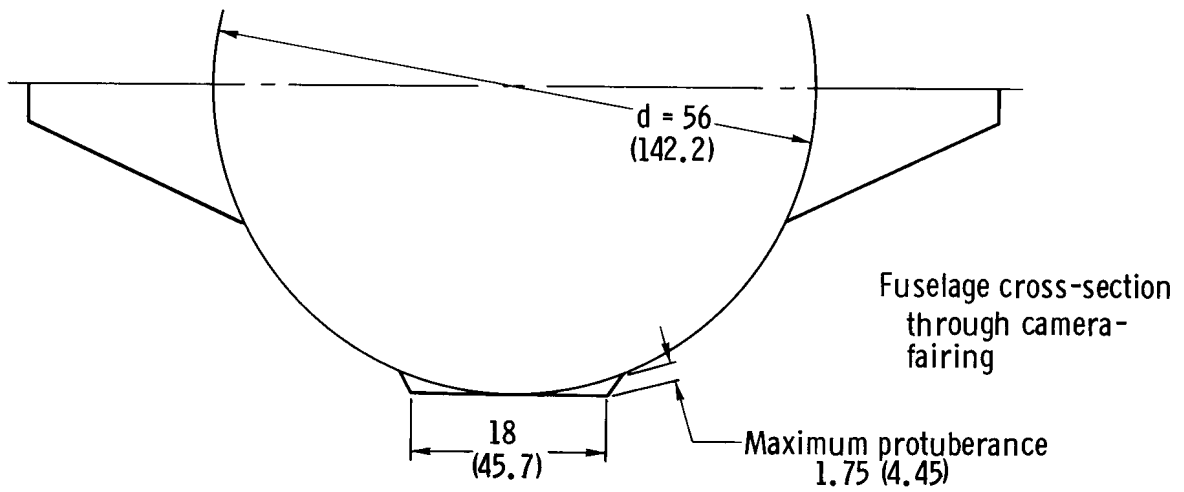


Figure 6.— Photograph and cross-sectional drawing of the camera fairing on the X-15-2 lower fuselage. All dimensions in inches (centimeters).

E-19092

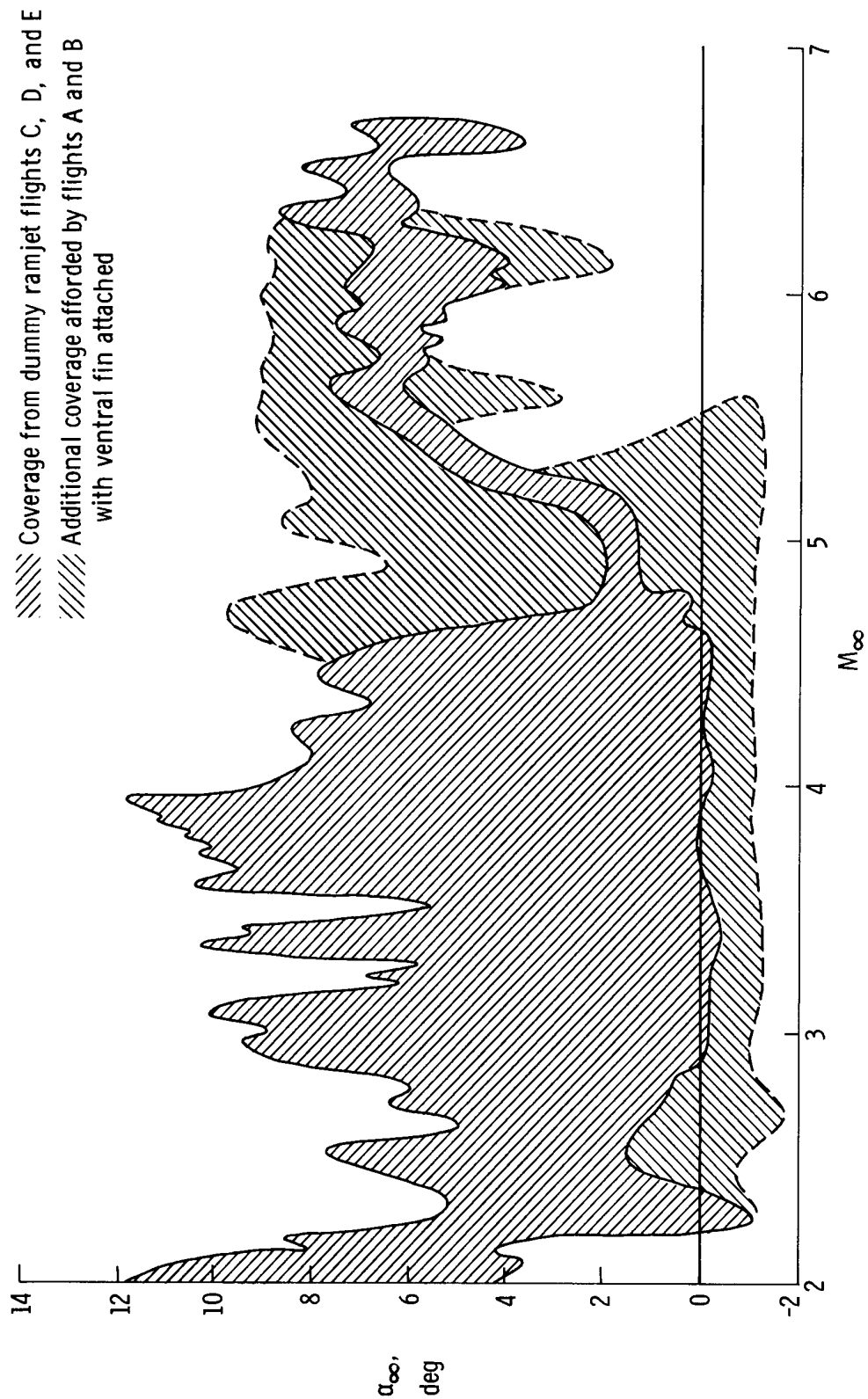


Figure 7. — Mach number and angle-of-attack coverage for the ramjet flow-field test flights.

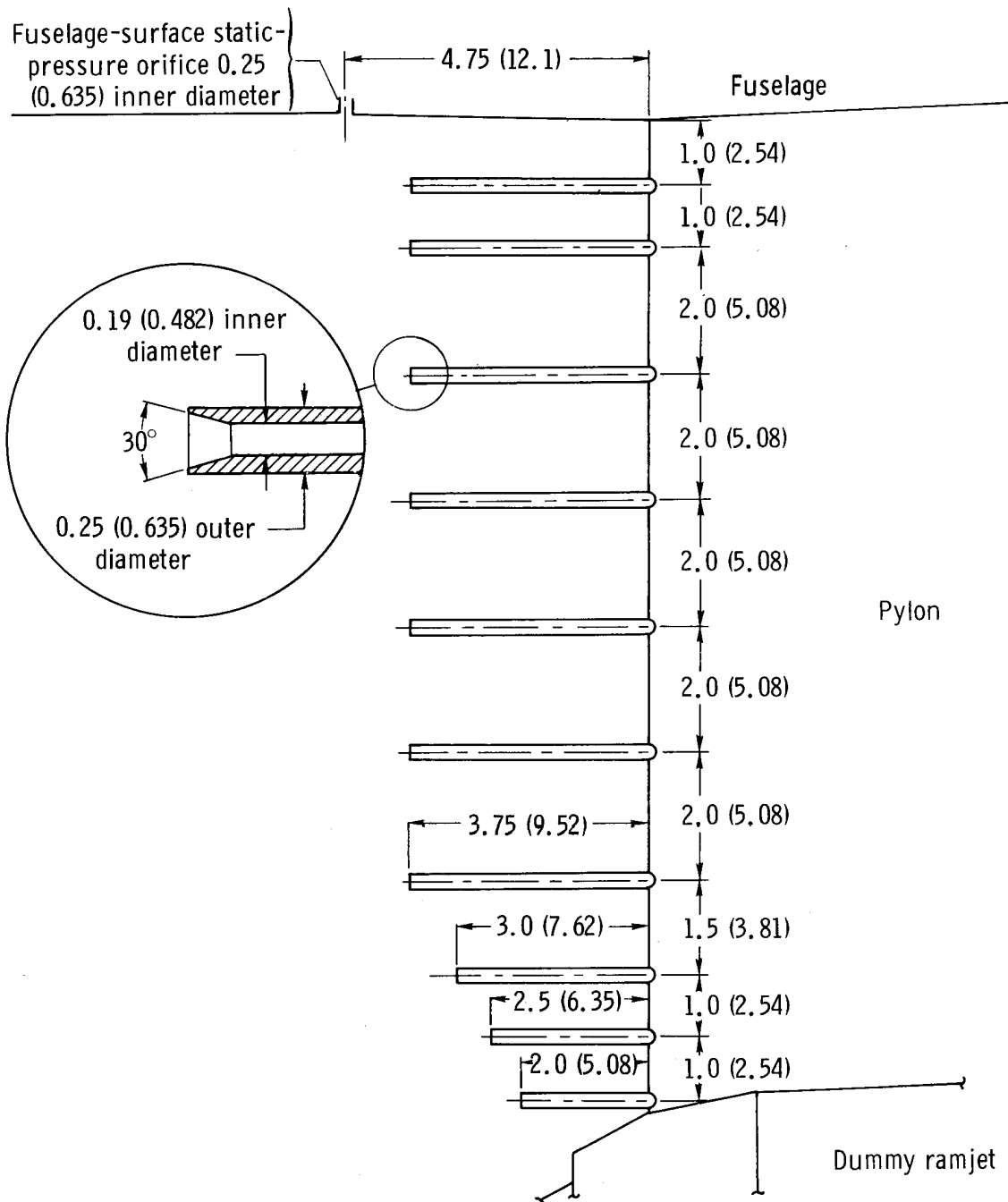


Figure 8.— Pylon-leading-edge impact-pressure probes. All dimensions in inches (centimeters) except as noted.

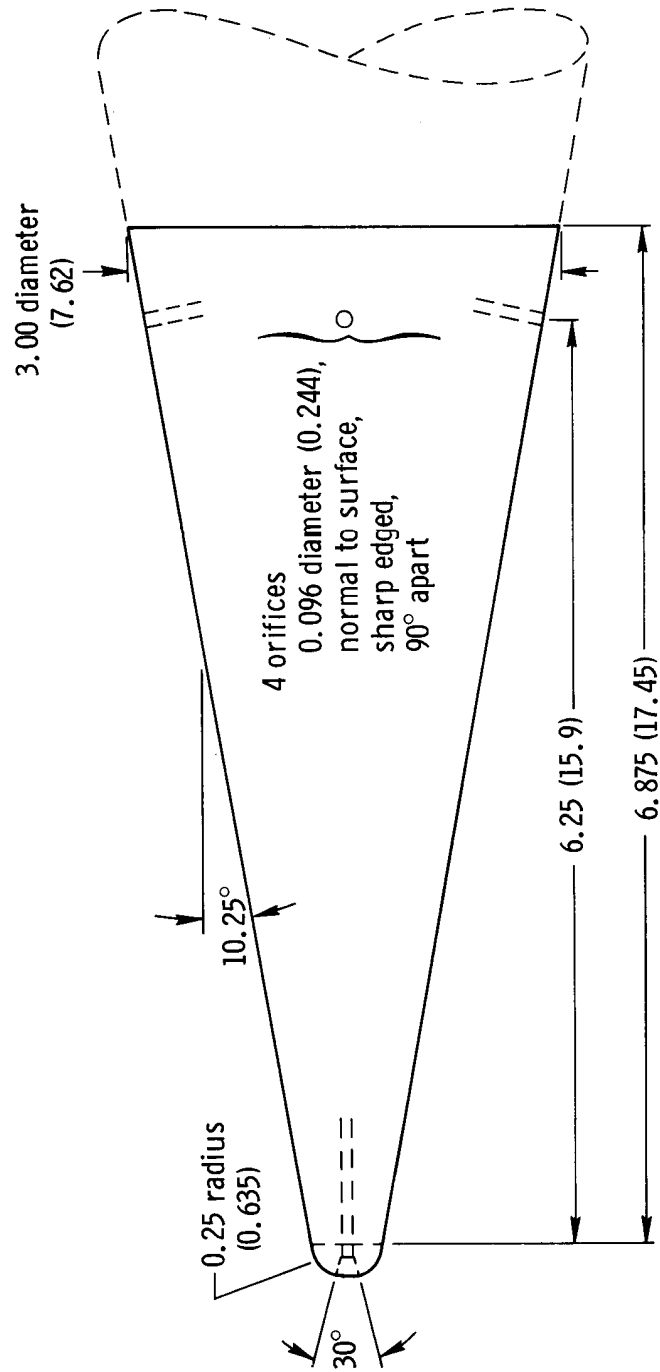
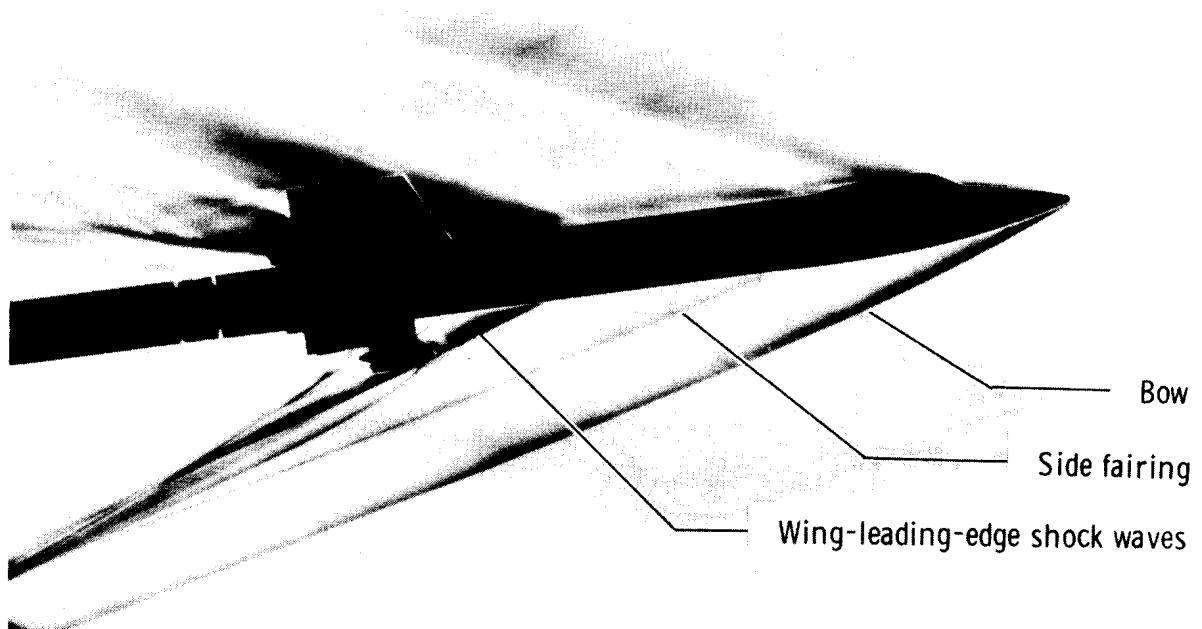
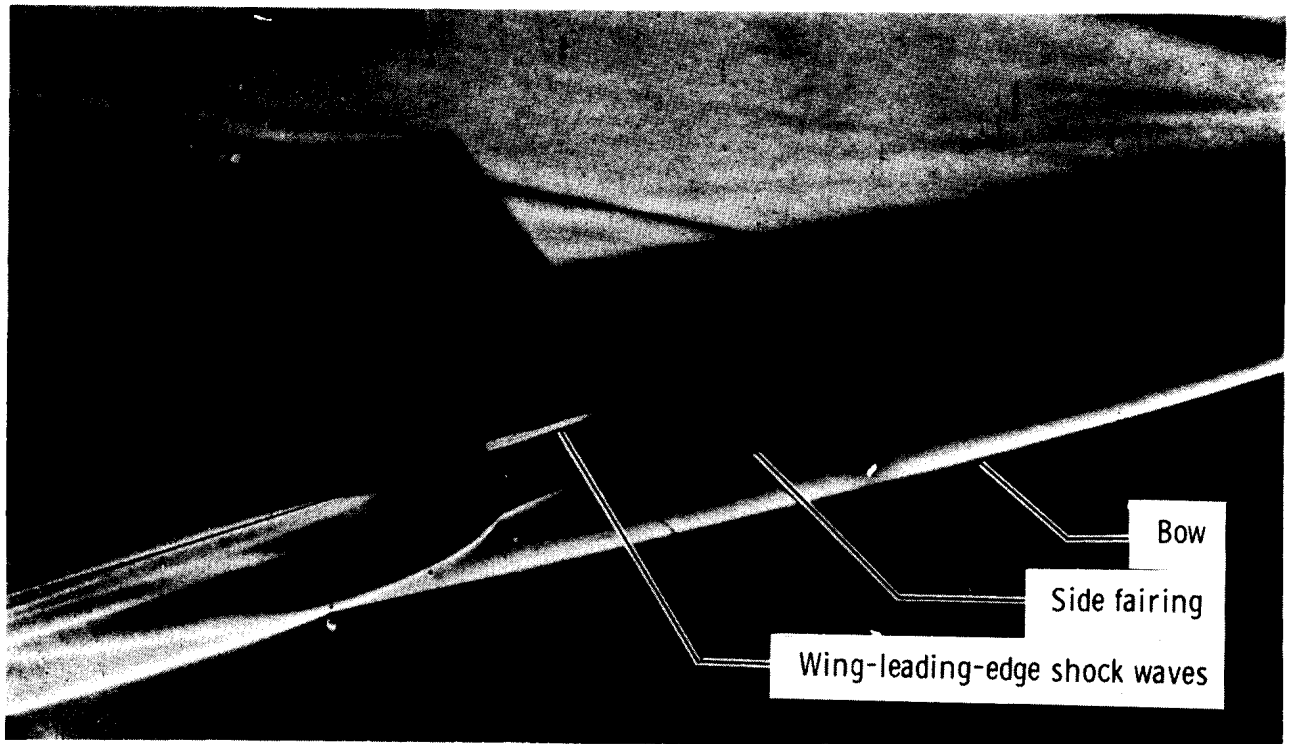


Figure 9.— Drawing of the 20° nose cone on the dummy ramjet showing pressure-orifice locations. All dimensions in inches (centimeters) except as noted.



(a) $M_{\infty} = 3.0$; $\alpha_{\infty} = 4^{\circ}$.



(b) $M_{\infty} = 6.7$; $\alpha_{\infty} = 8^{\circ}$.

Figure 10.— Wind-tunnel schlieren photographs of the X-15-2 with the dummy ramjet installed.

Data source	Reference data				Present data			
	Wind tunnel (ref. 2)	Wind tunnel (ref. 2)	Theory (ref. 5)	Flight (ref. 4)	20° nose cone or 40° center cone	Lower 40° cone probe	Ventral impact-pressure probe	Pylon impact probes
Parameter presented	M_L, α_L	$\frac{p_{iL}}{p_{i\infty}}$	M_L, α_L	$\frac{p_{iL}}{p_{i\infty}}$	$\frac{p_{iL}}{p_{i\infty}}, M_L, \alpha_L$	$\frac{p_{iL}}{p_{i\infty}}, M_L, \alpha_L$	$\frac{p_{iL}}{p_{i\infty}}$	$\frac{p_{iL}}{p_{i\infty}}$
$\frac{x}{d}$	7.37	7.77	7.77	8.05	8.55	8.55	8.74	9.15
$\frac{z}{d}$	0 to 1	0 to 1	0 to 2	0.22	0.45	0.60	0.39	0.02 to 0.28

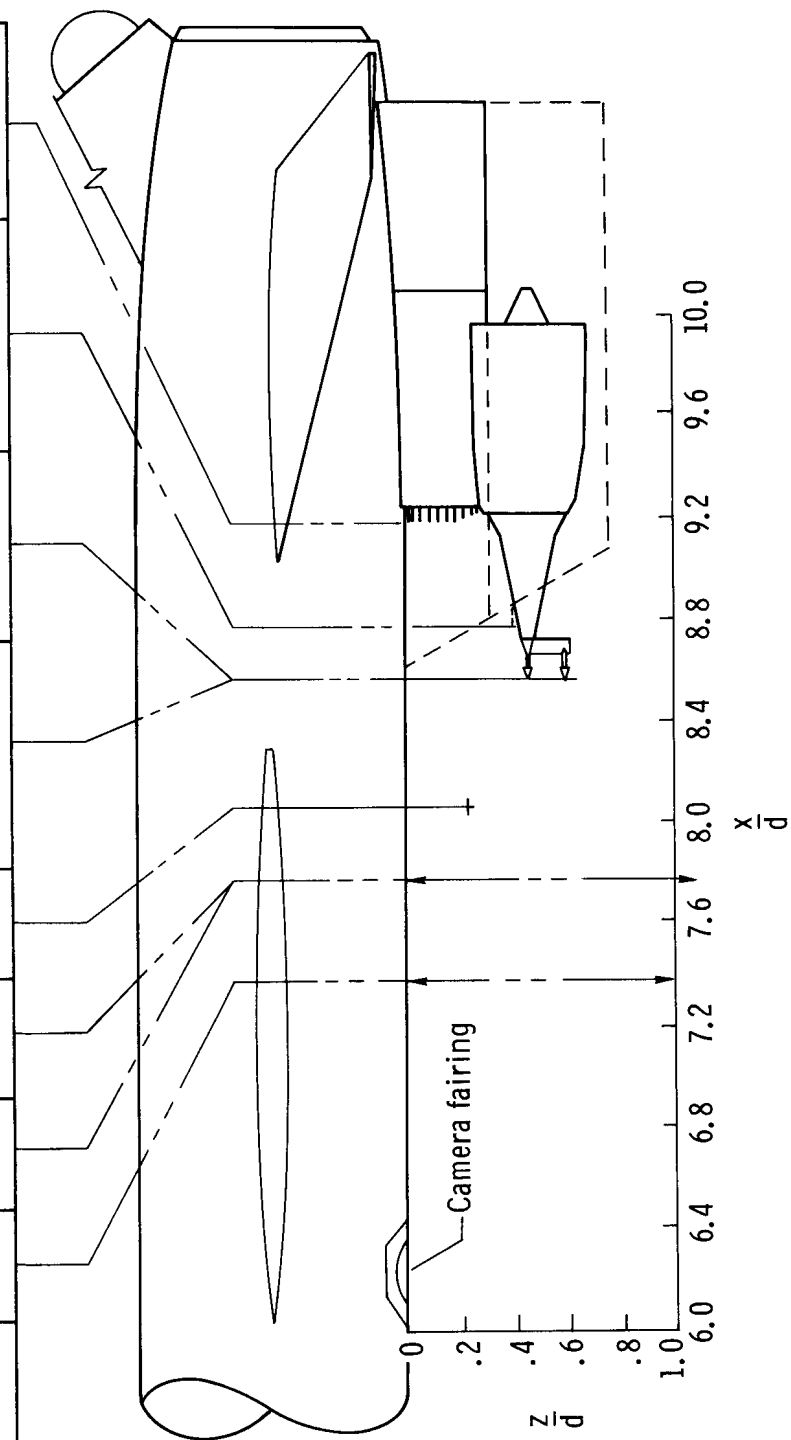
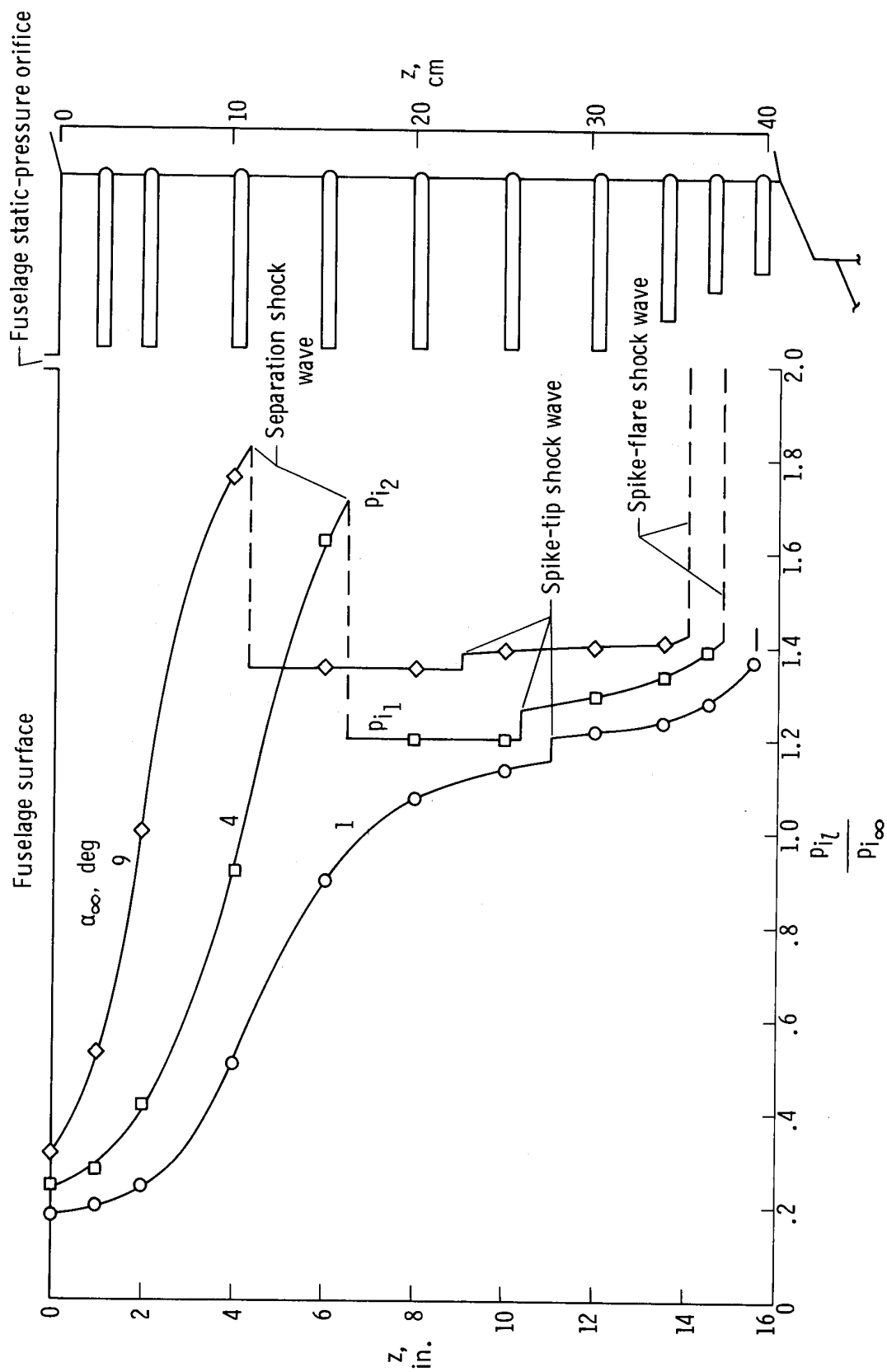
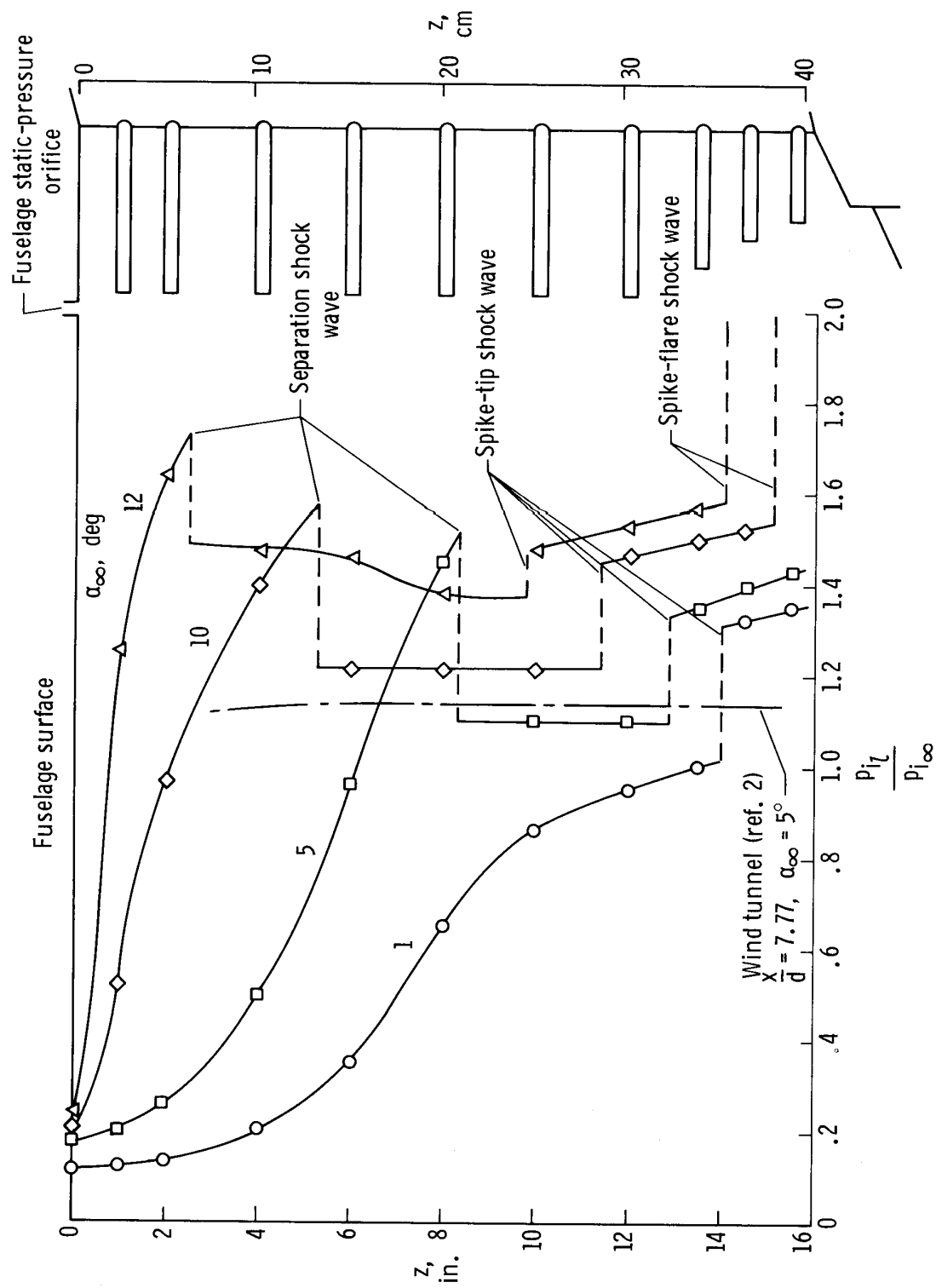


Figure 11. — Flow-field survey stations for flight and wind-tunnel tests and theoretical calculations.



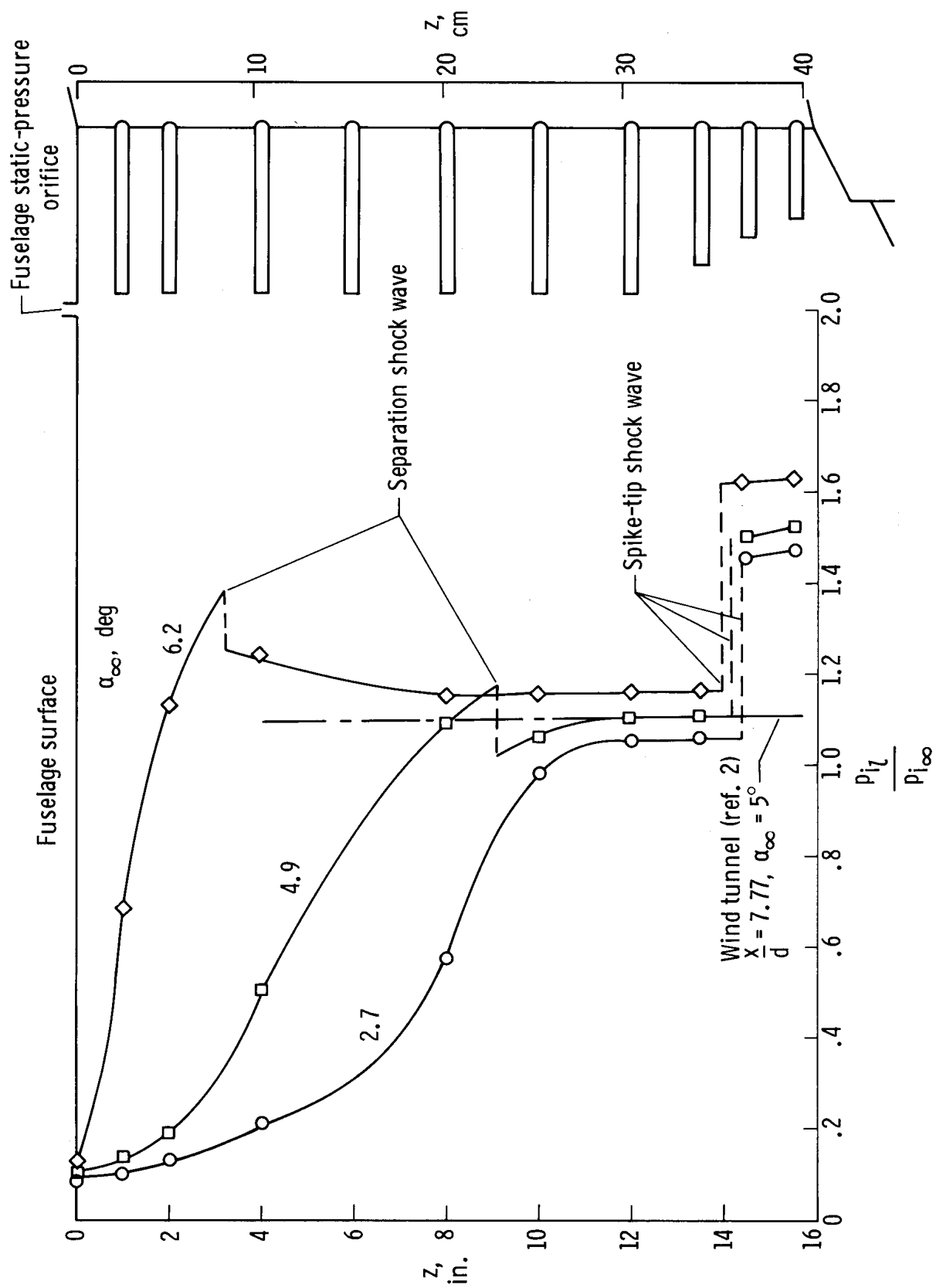
(a) $M_\infty = 3.0$.

Figure 12.— Effect of angle of attack and Mach number on pylon impact pressure at $\beta_\infty = 0.5^\circ$.



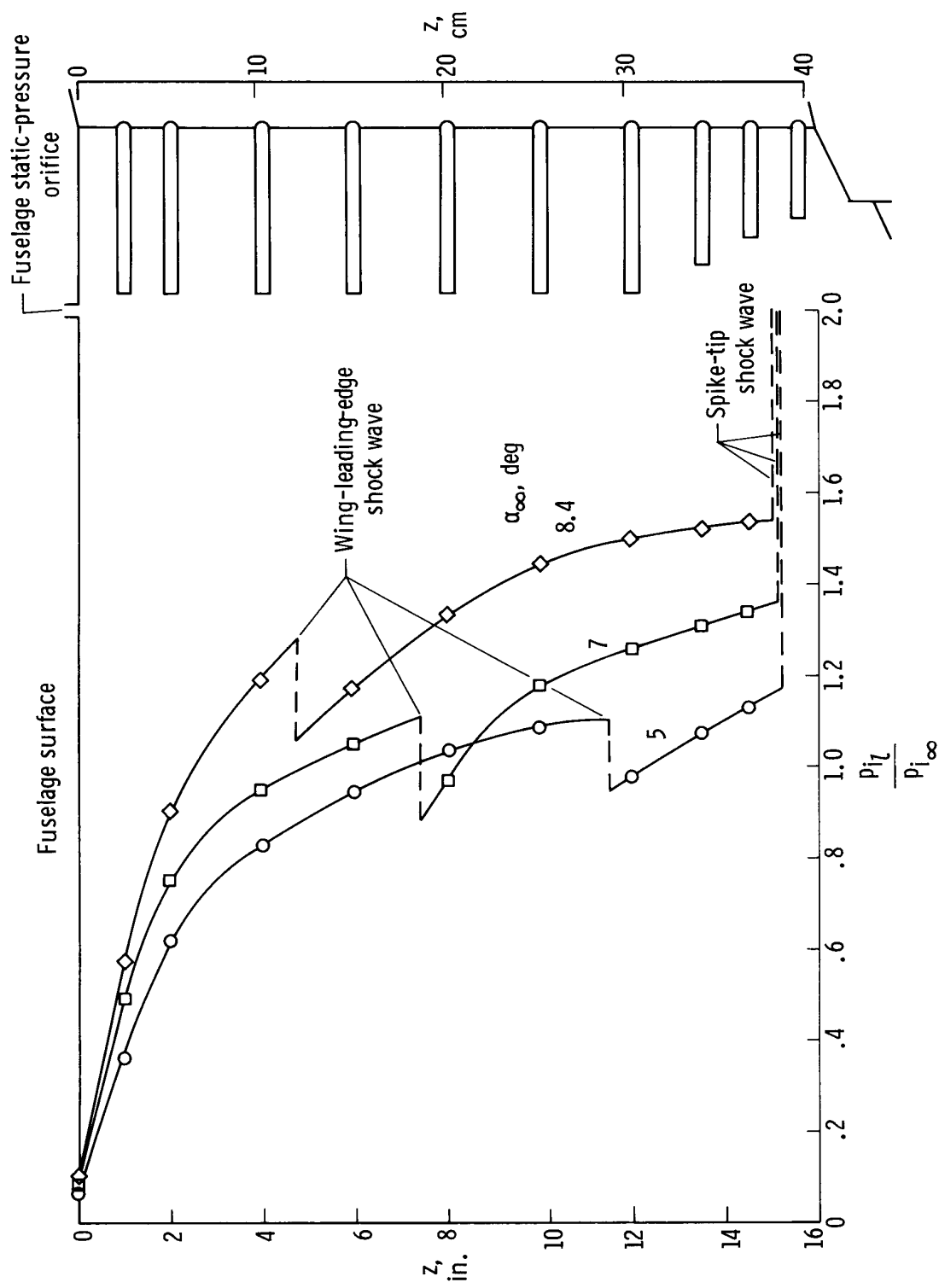
(b) $M_\infty = 4.0$.

Figure 12. - Continued.



(c) $M_\infty = 4.65$.

Figure 12. - Continued.



(d) $M_\infty = 6.5$.

Figure 12. — Concluded.

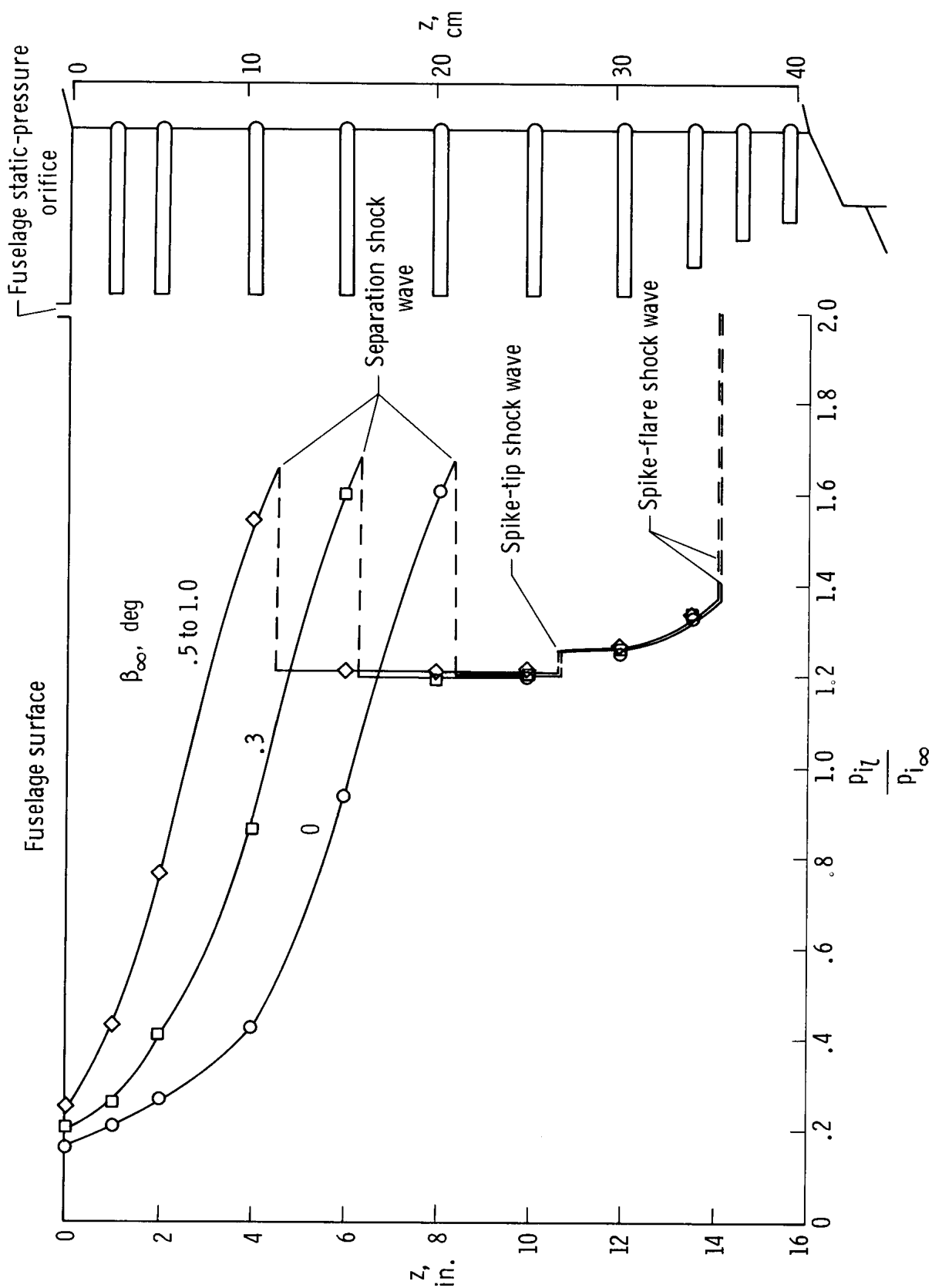


Figure 13.— Effect of angle of sideslip on pylon impact-pressure profiles at $M_\infty = 3.0$ and $\alpha_\infty = 5^\circ$.

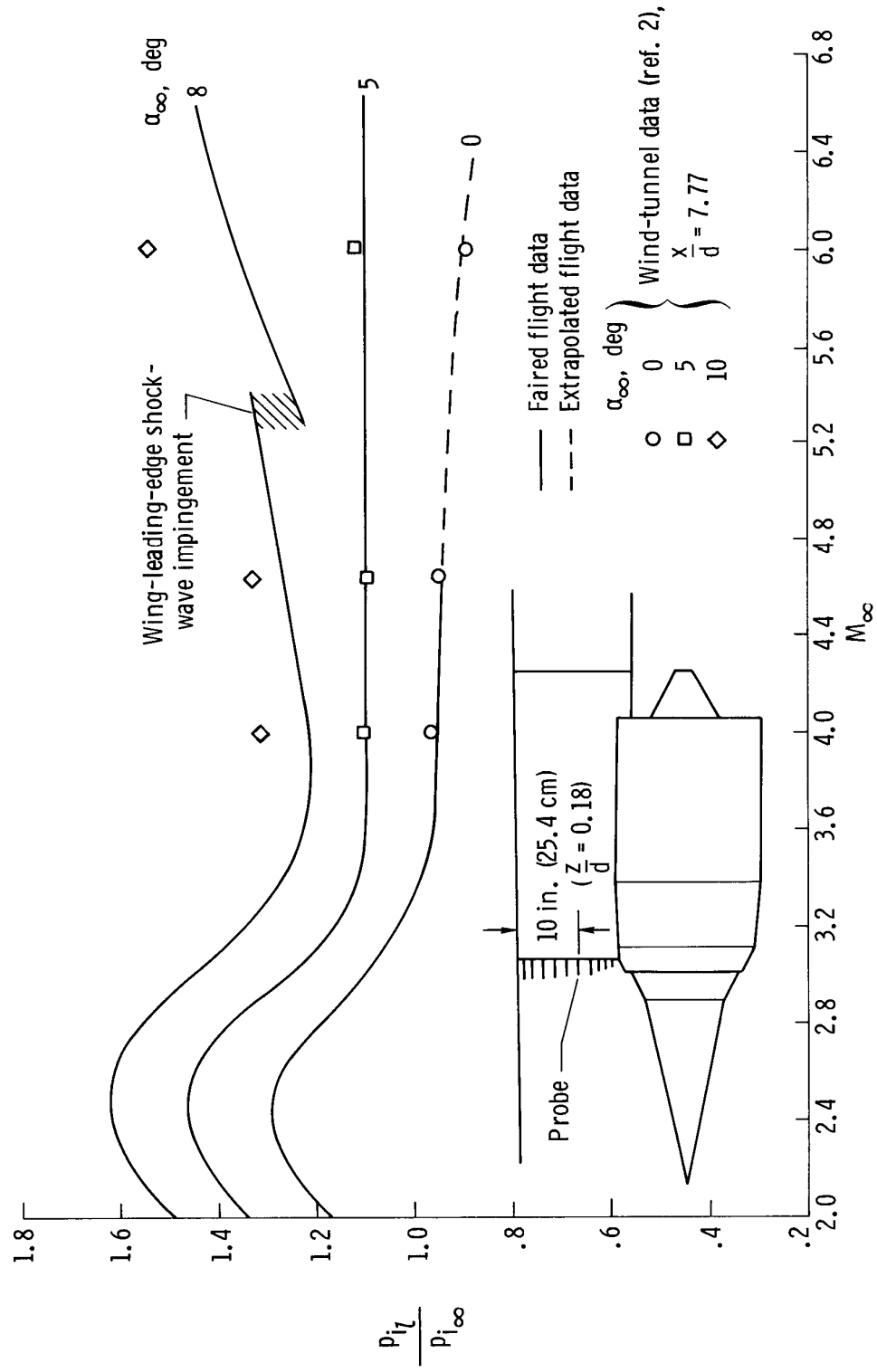


Figure 14. - Variation of impact-pressure ratio at a probe in the middle of the pylon with M_∞ and α_∞ .

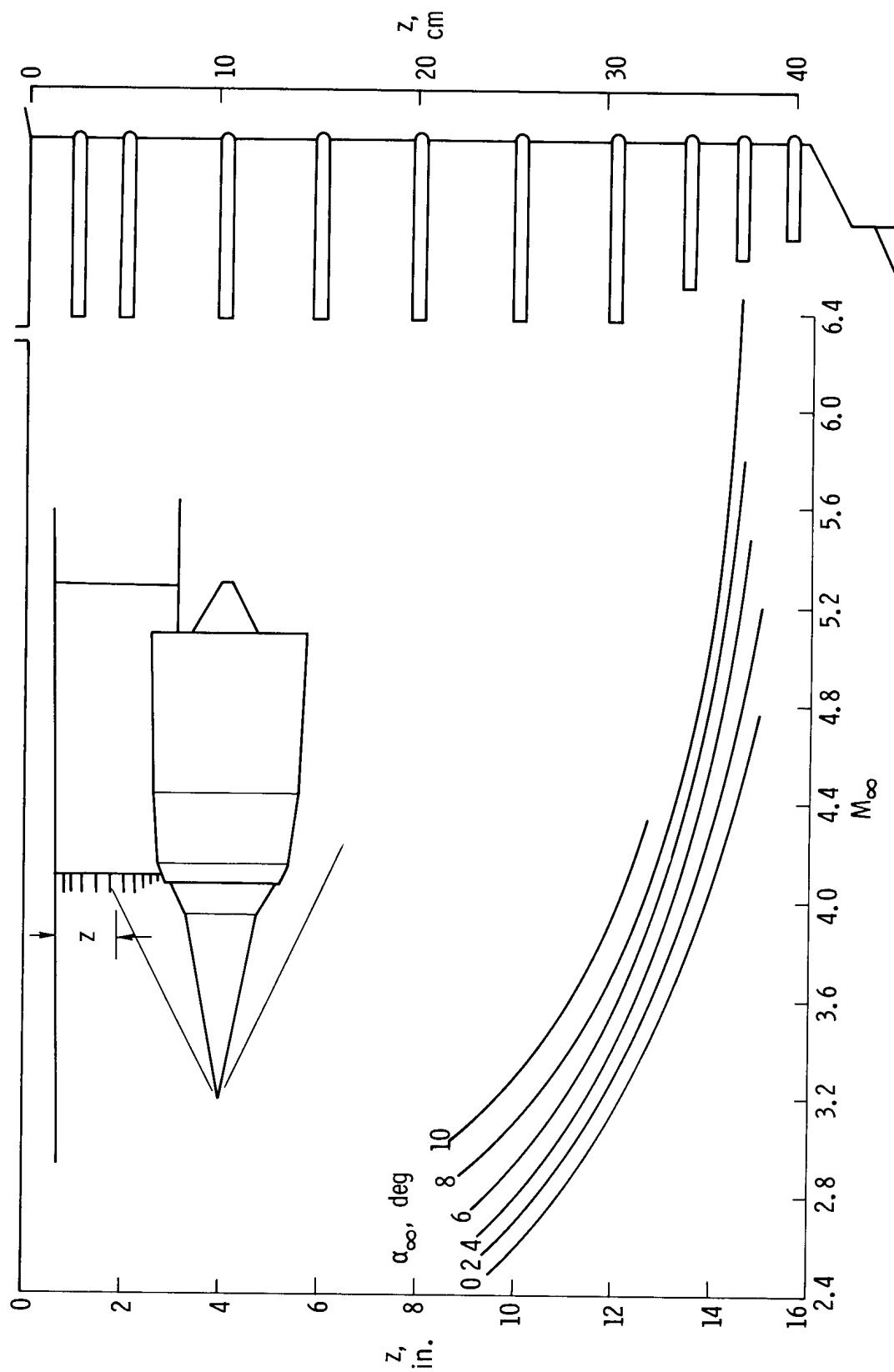


Figure 15. — Effect of Mach number and angle of attack on dummy ramjet spike-tip shock-wave position on pylon.

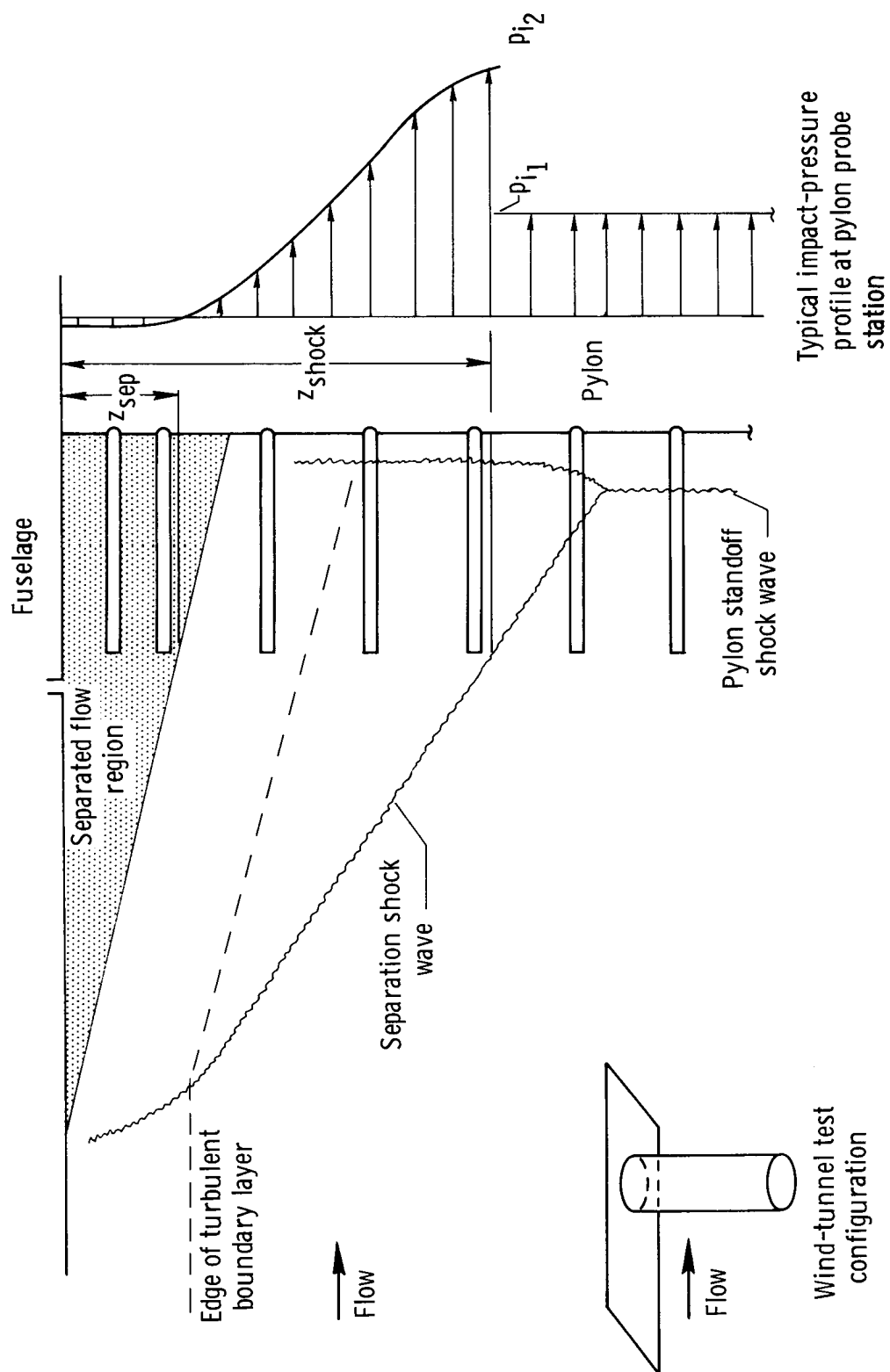


Figure 16. – Pylon-fuselage intersection flow model.

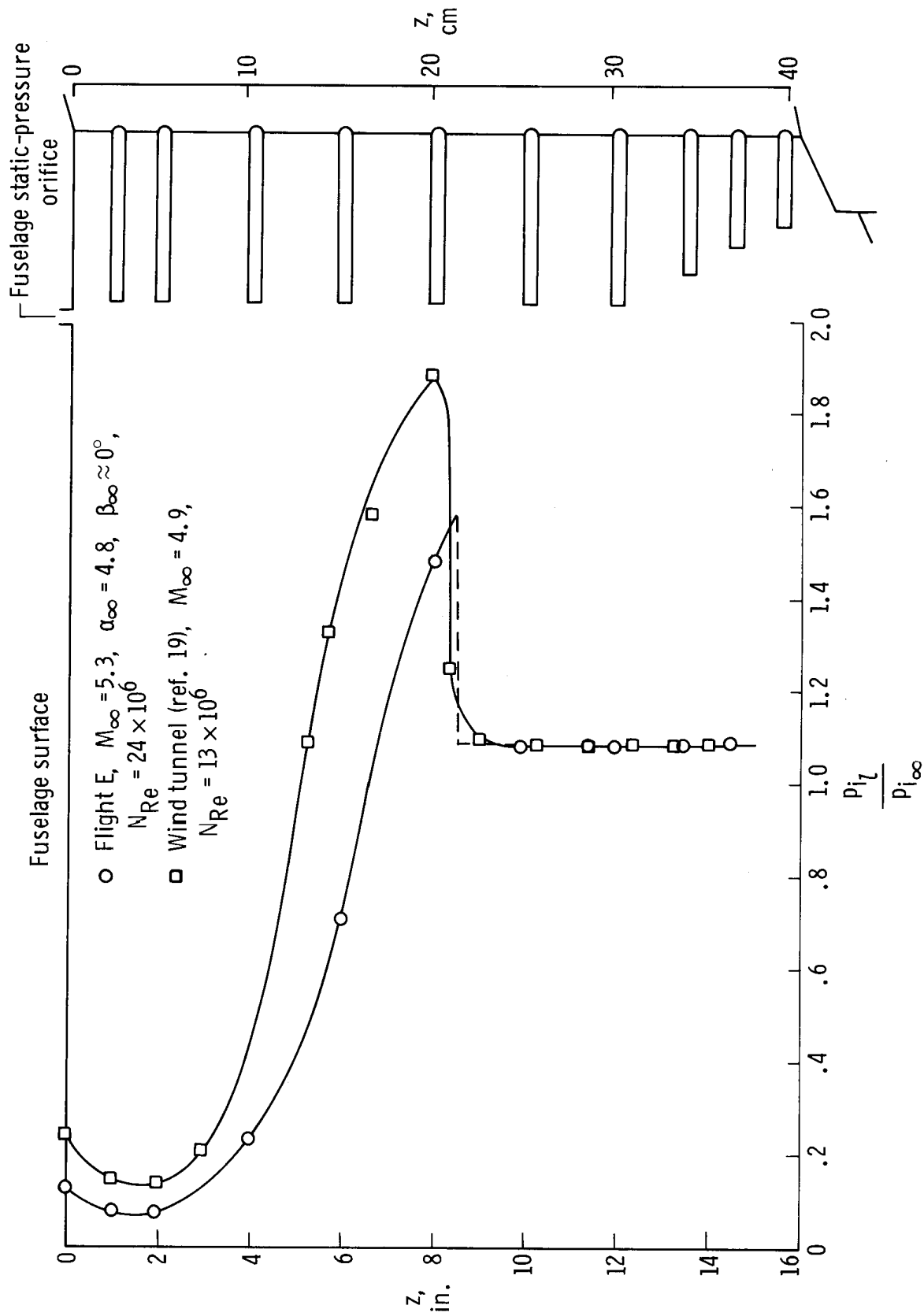


Figure 17.- Comparison of flight pylon impact-pressure data with wind-tunnel pressure data on a cylinder normal to a flat plate.

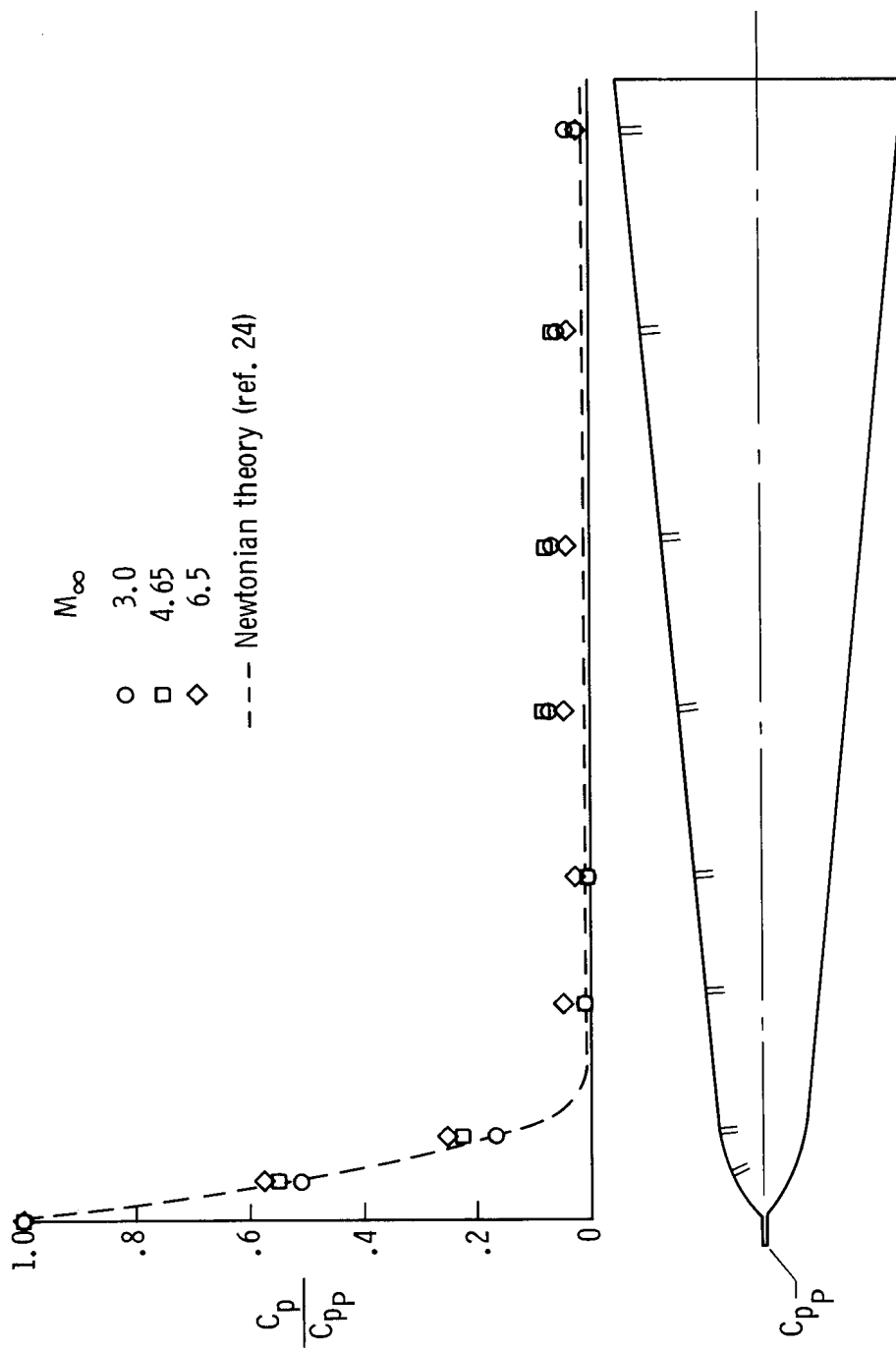
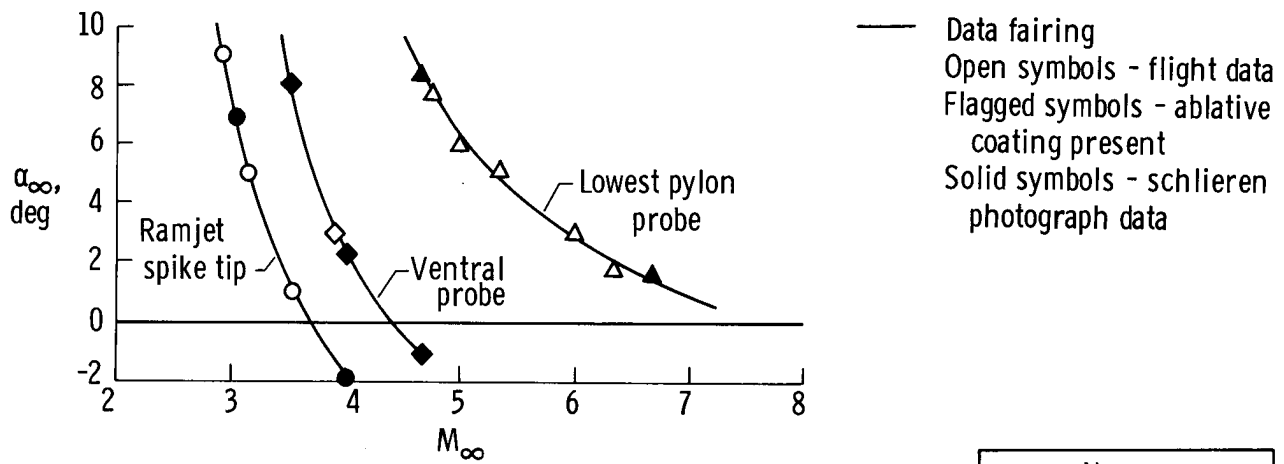
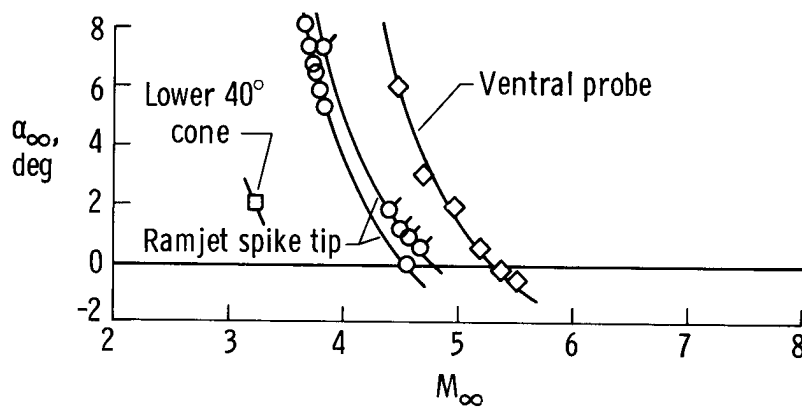


Figure 18.— Pylon surface pressure-coefficient ratios. $\beta \approx 0^\circ$.



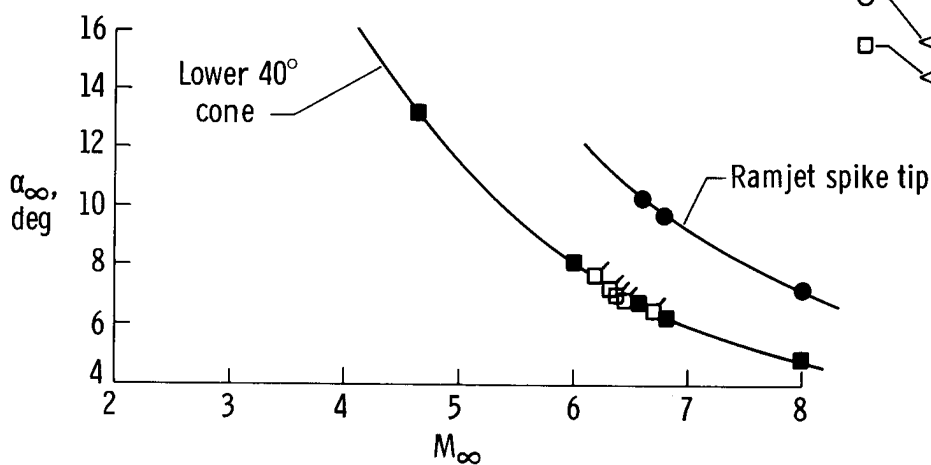
(a) Wing-leading-edge shock-wave impingement.

	N_{Re}	
	Flight	Wind tunnel
Maximum	50×10^6	12.5×10^6
Minimum	20×10^6	2.7×10^6



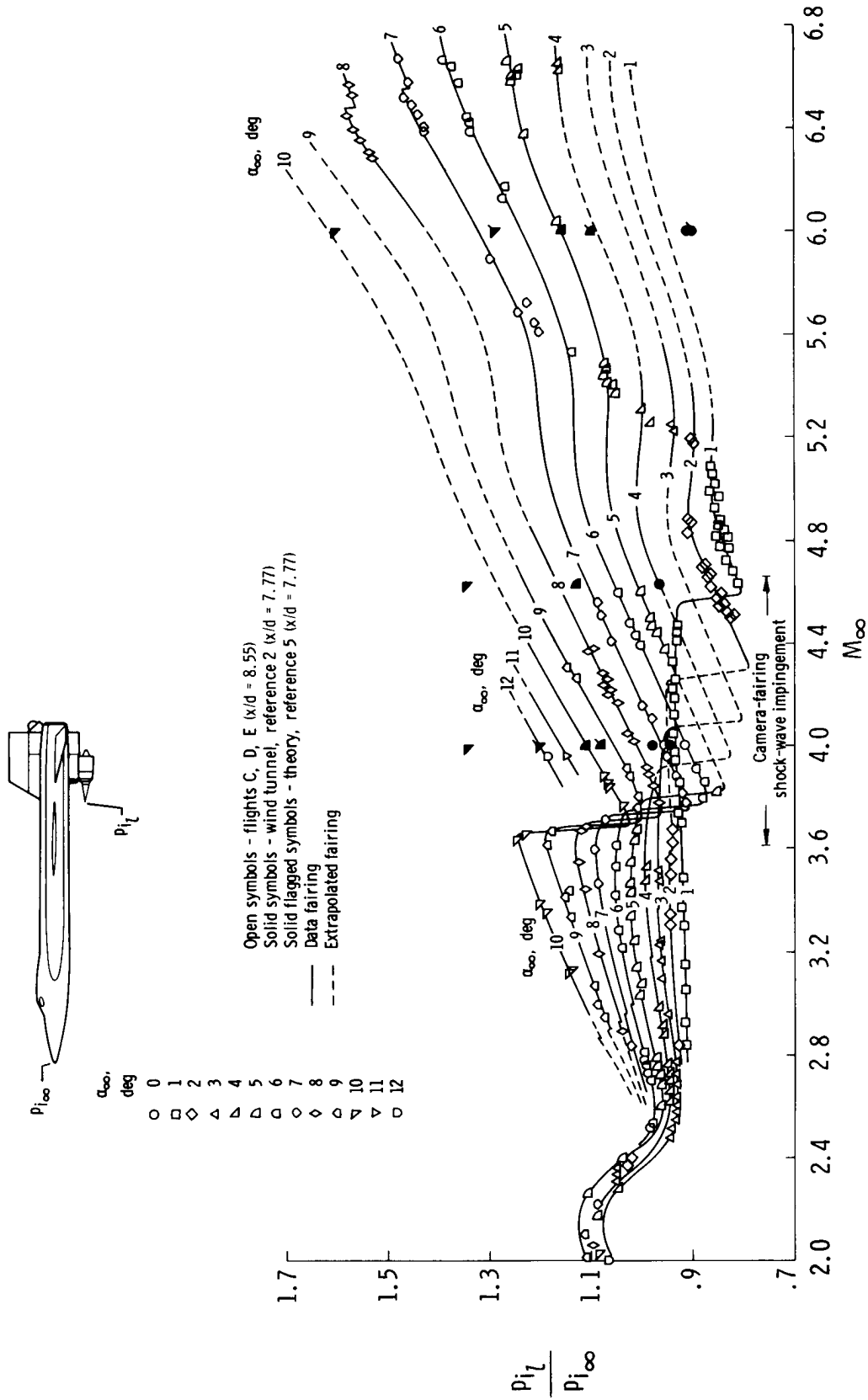
(b) Camera-fairing shock-wave impingement.

For probe locations, see figure 11



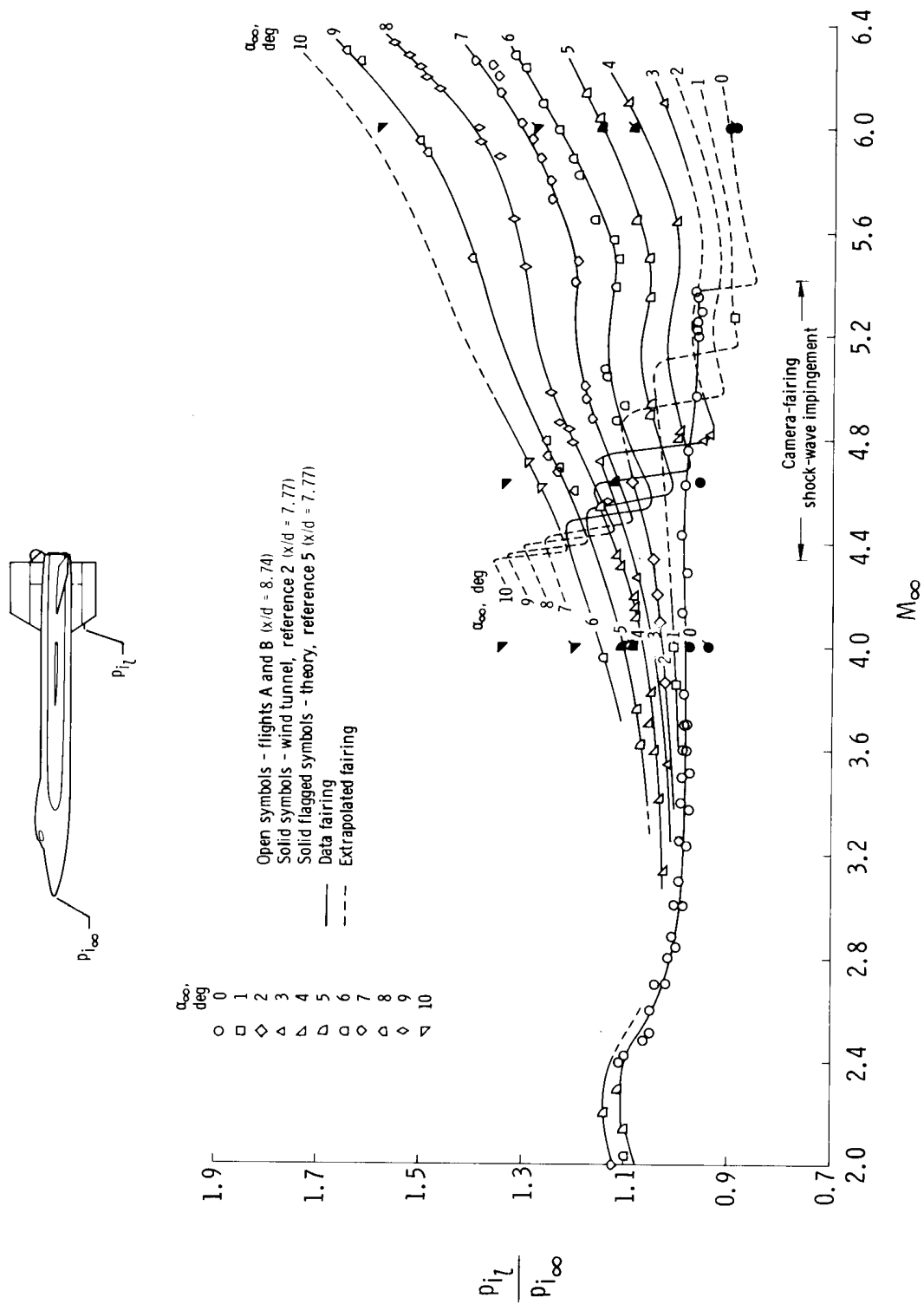
(c) Fuselage side-fairing shock-wave impingement.

Figure 19.— Effect of M_{∞} and α_{∞} on shock-wave impingement in the ramjet region.



(a) Ramjet spike tip.

Figure 20.— Effect of M_{∞} and α_{∞} on the impact-pressure ratio in the ramjet region.



(b) Ventral impact-pressure probe.

Figure 20. - Concluded.

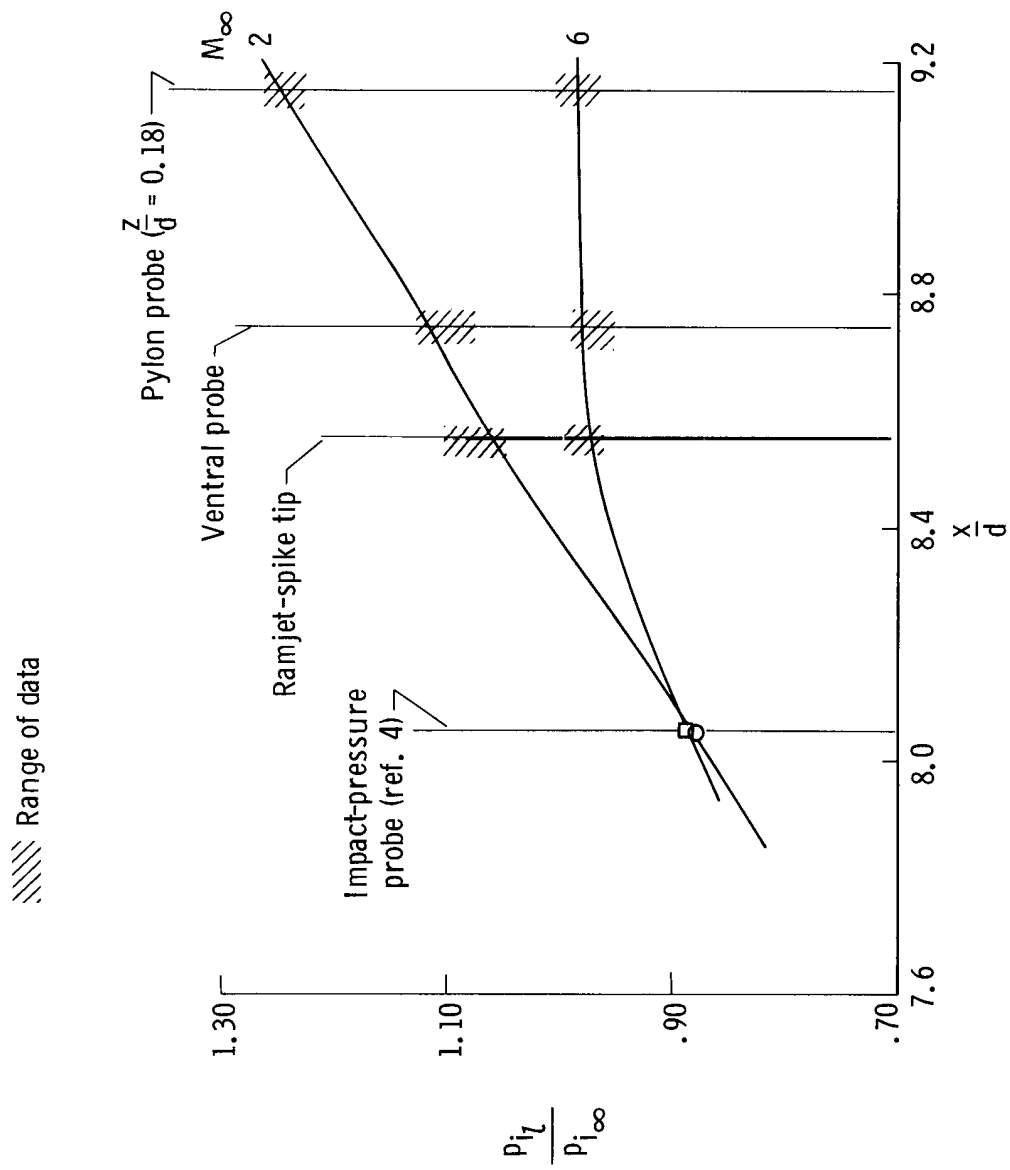
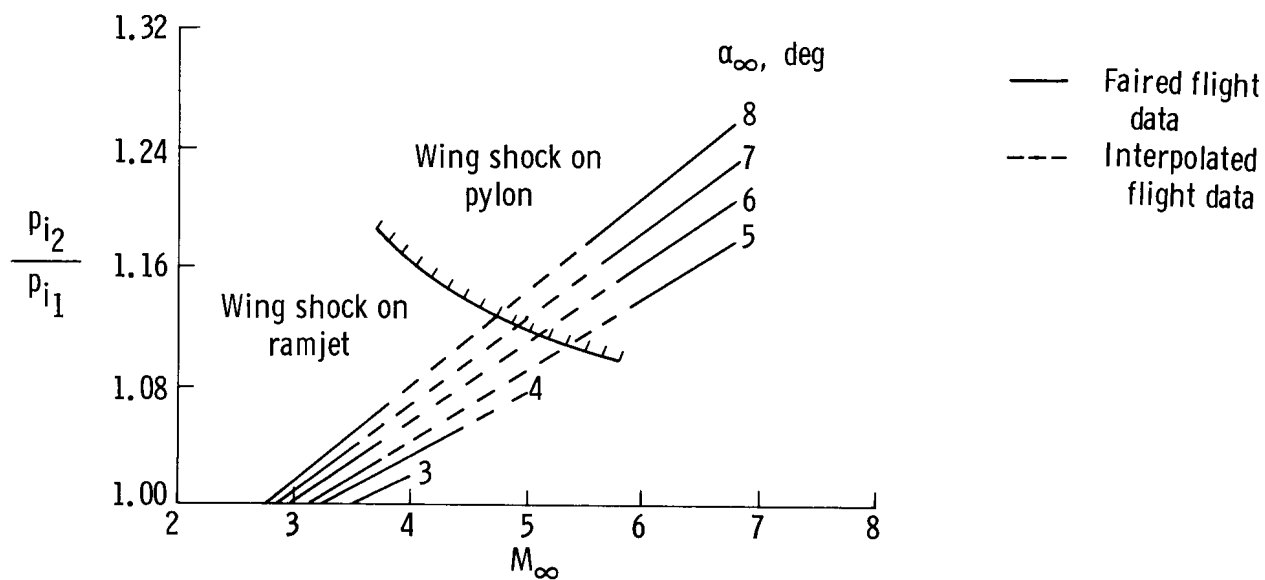
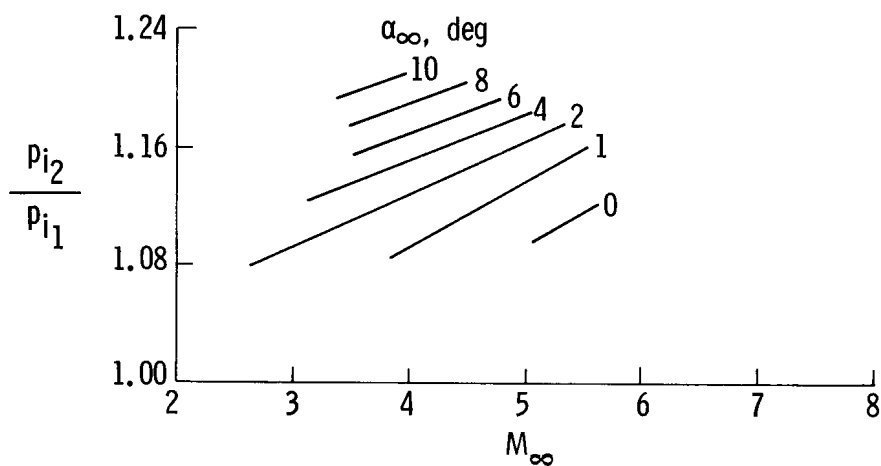


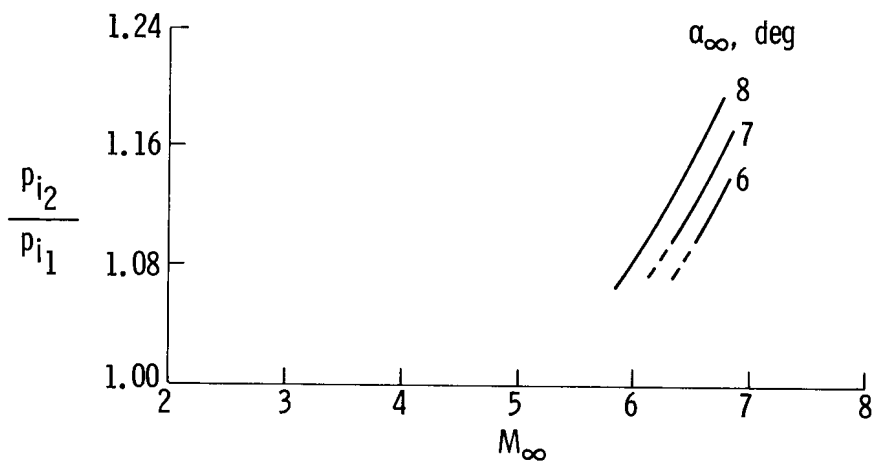
Figure 21. — Effect of fuselage station $\frac{x}{d}$ on flight impact-pressure ratio for $\alpha_\infty = 2^\circ$.



(a) Wing-leading-edge shock wave.



(b) Camera-fairing shock wave.



(c) Fuselage side-fairing shock wave.

Figure 22.— Effect of M_∞ and α_∞ on the strength of the impinging shock waves on the ramjet and pylon.

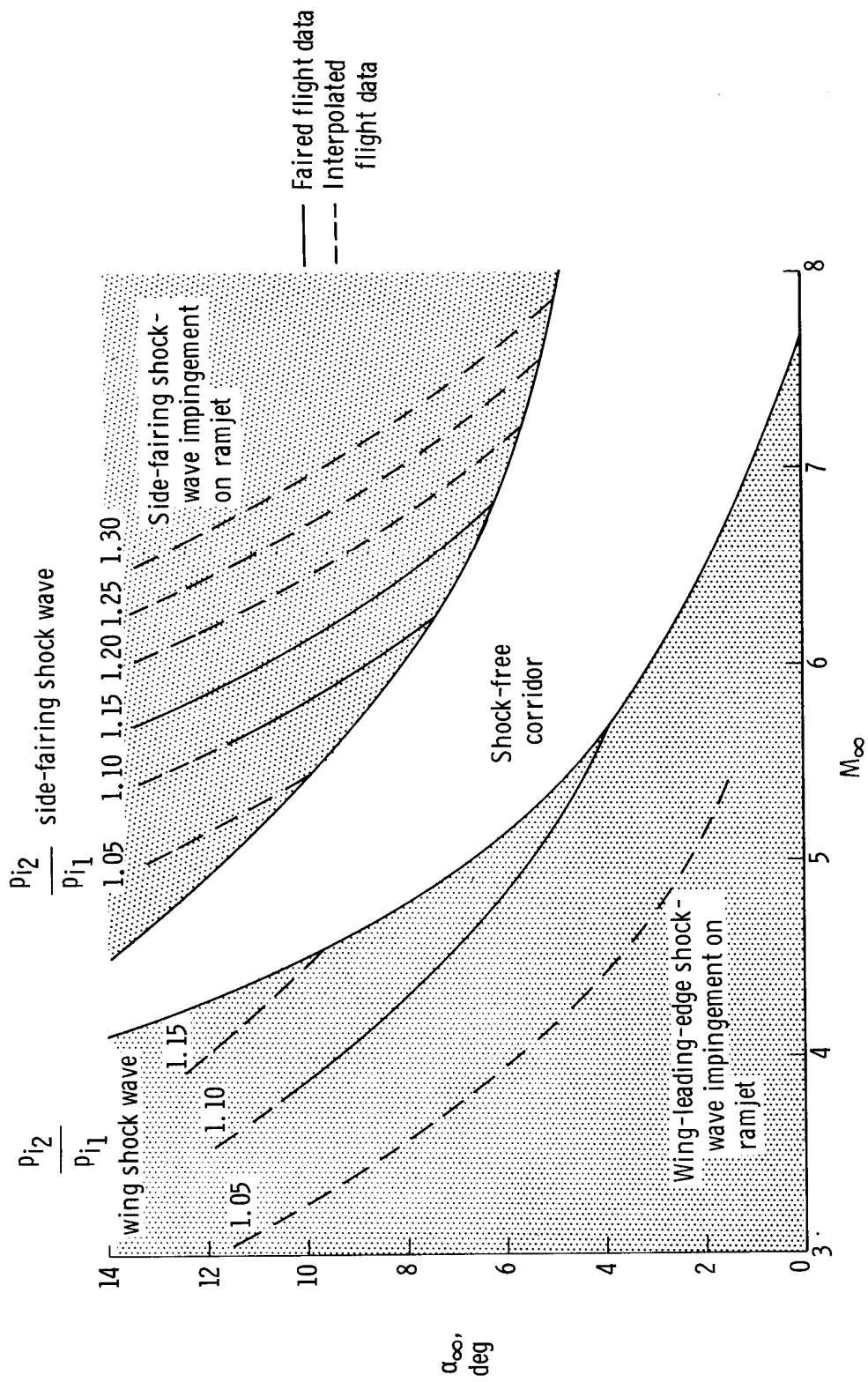


Figure 23.— Effect of M_∞ and α_∞ on the flight-test corridor free of shock-wave impingement (assuming camera fairing removed).

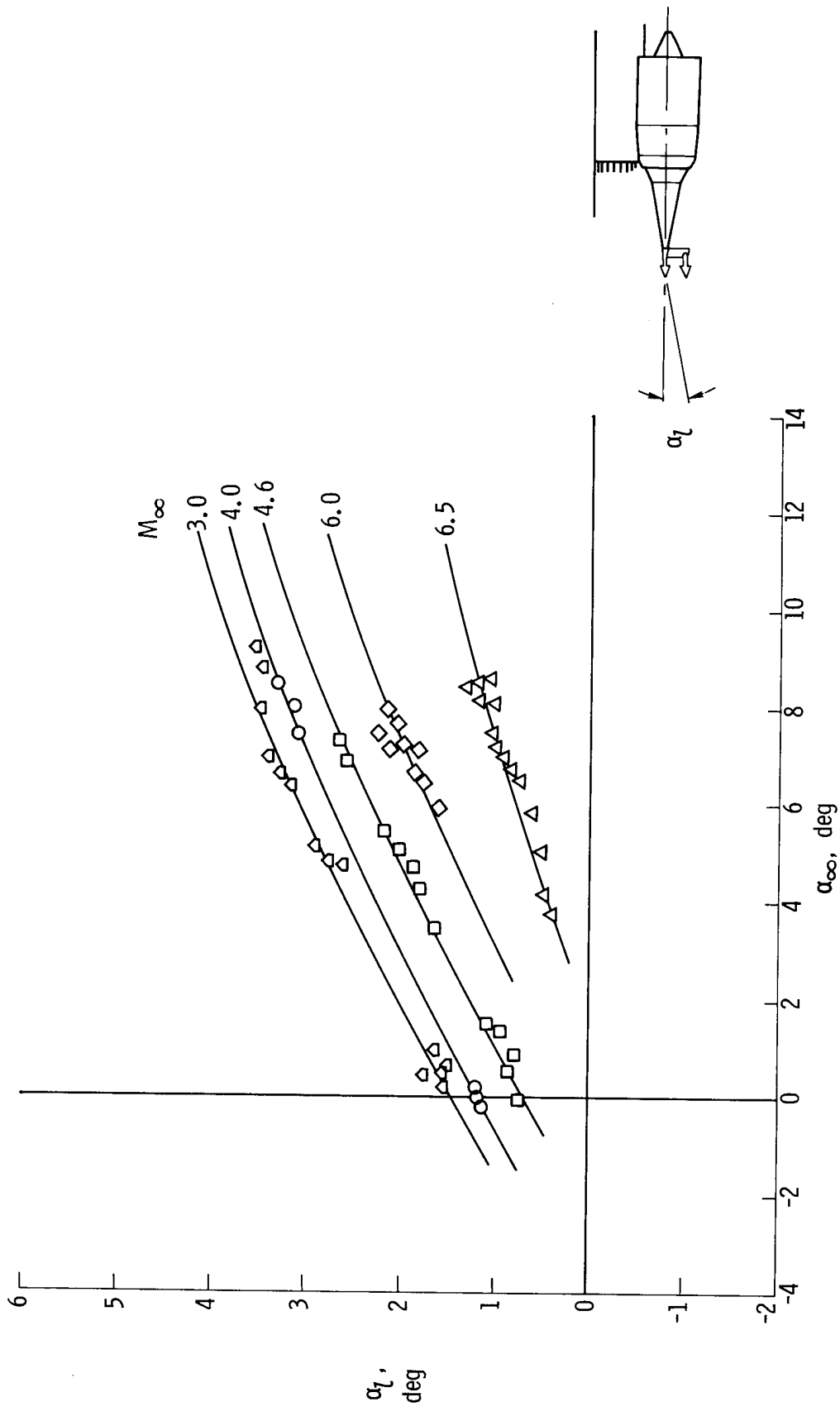
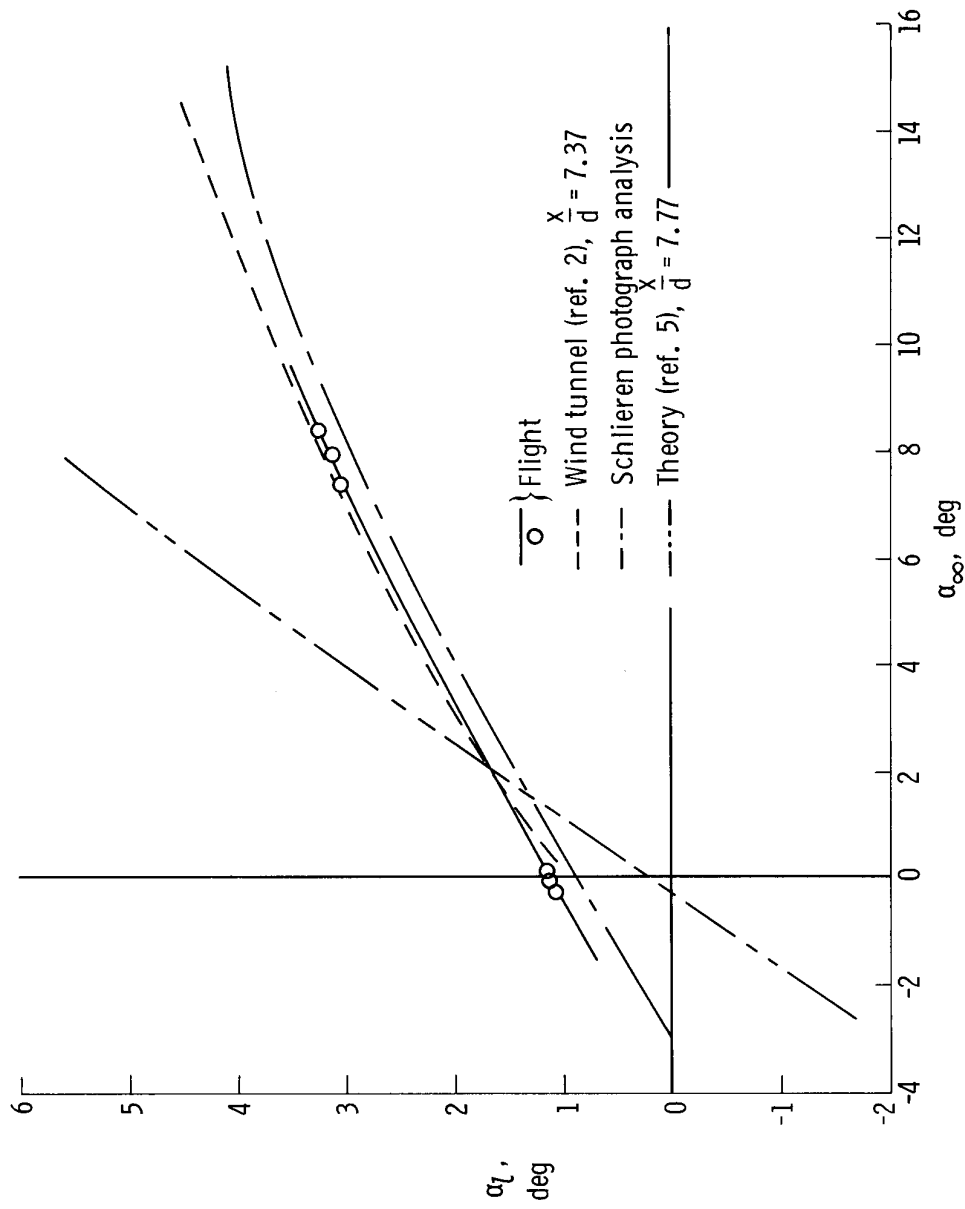
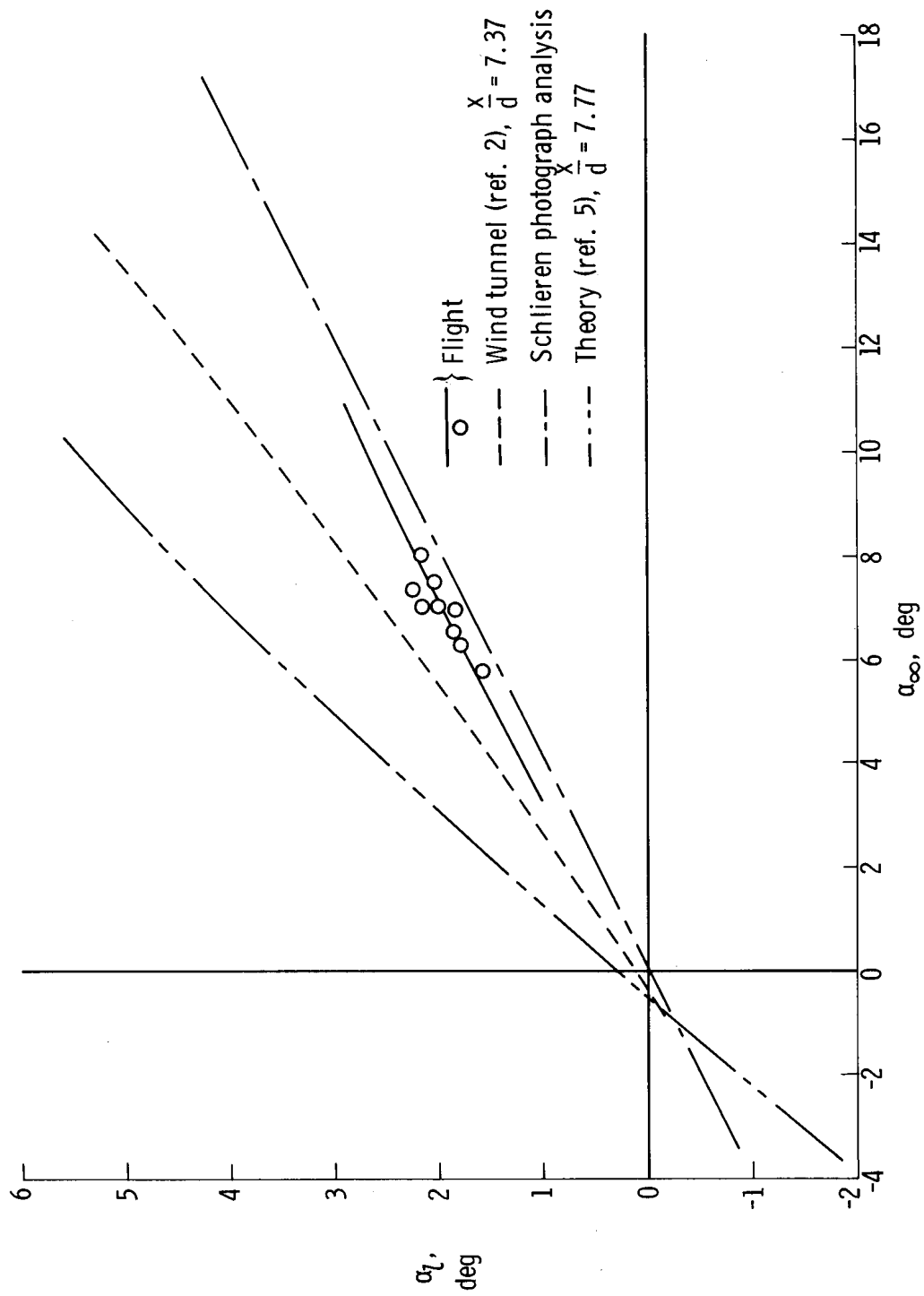


Figure 24.— Variation with M_∞ and α_∞ of the local angle of attack at the dummy ramjet spike tip.



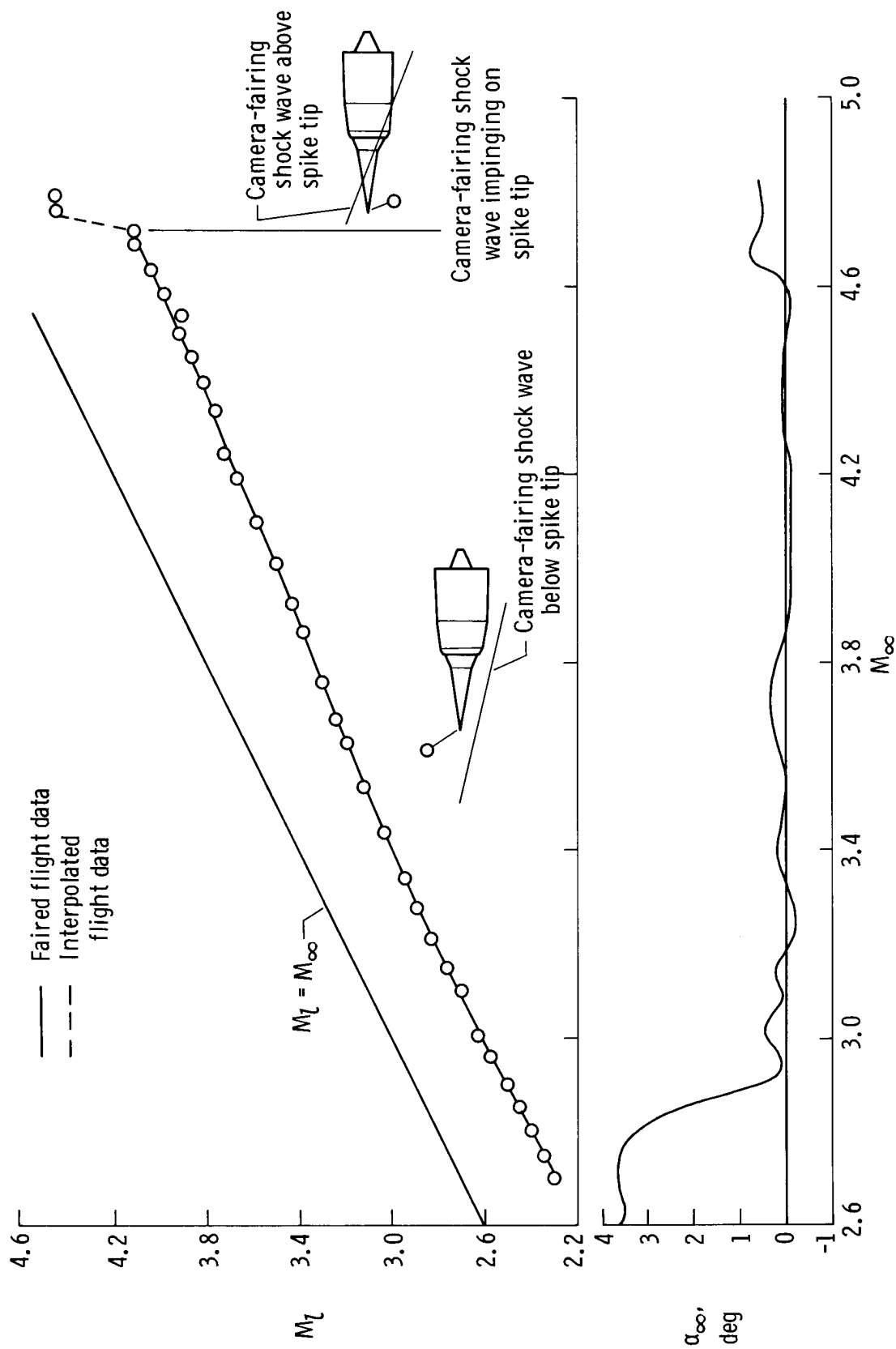
(a) $M_\infty = 4.0$.

Figure 25. — Comparison of α_L at the ramjet spike tip from flight, wind-tunnel schlieren photographs, and theoretical calculations.

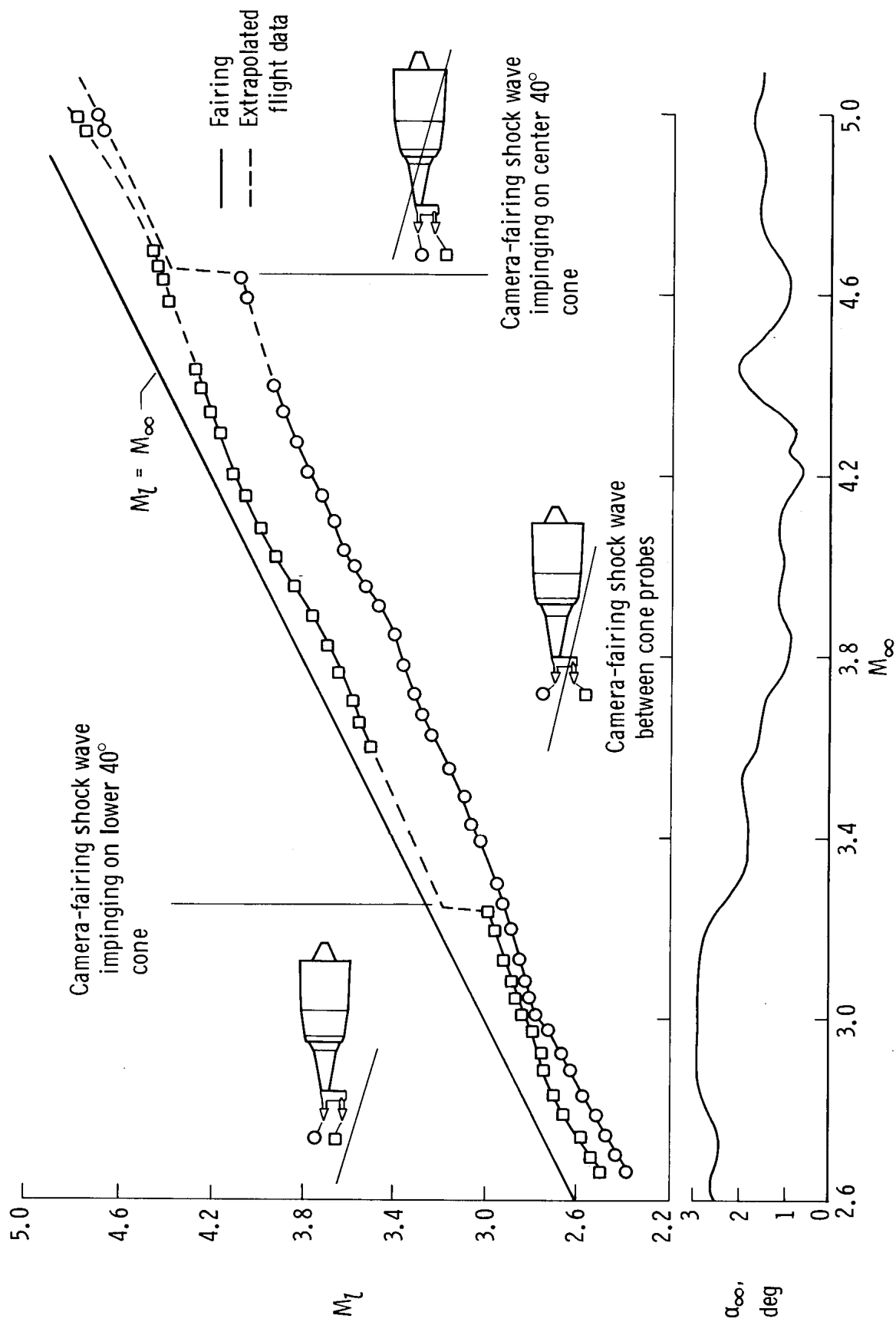


(b) $M_\infty = 6.0$.

Figure 25. -- Concluded.



(a) Ramjet 20° nose cone.
 Figure 26. — Effect of free-stream Mach number on local Mach number for free-stream angles of attack from 0° to 4°.



(b) Ramjet 40°-cone probe rake.

Figure 26. — Concluded.

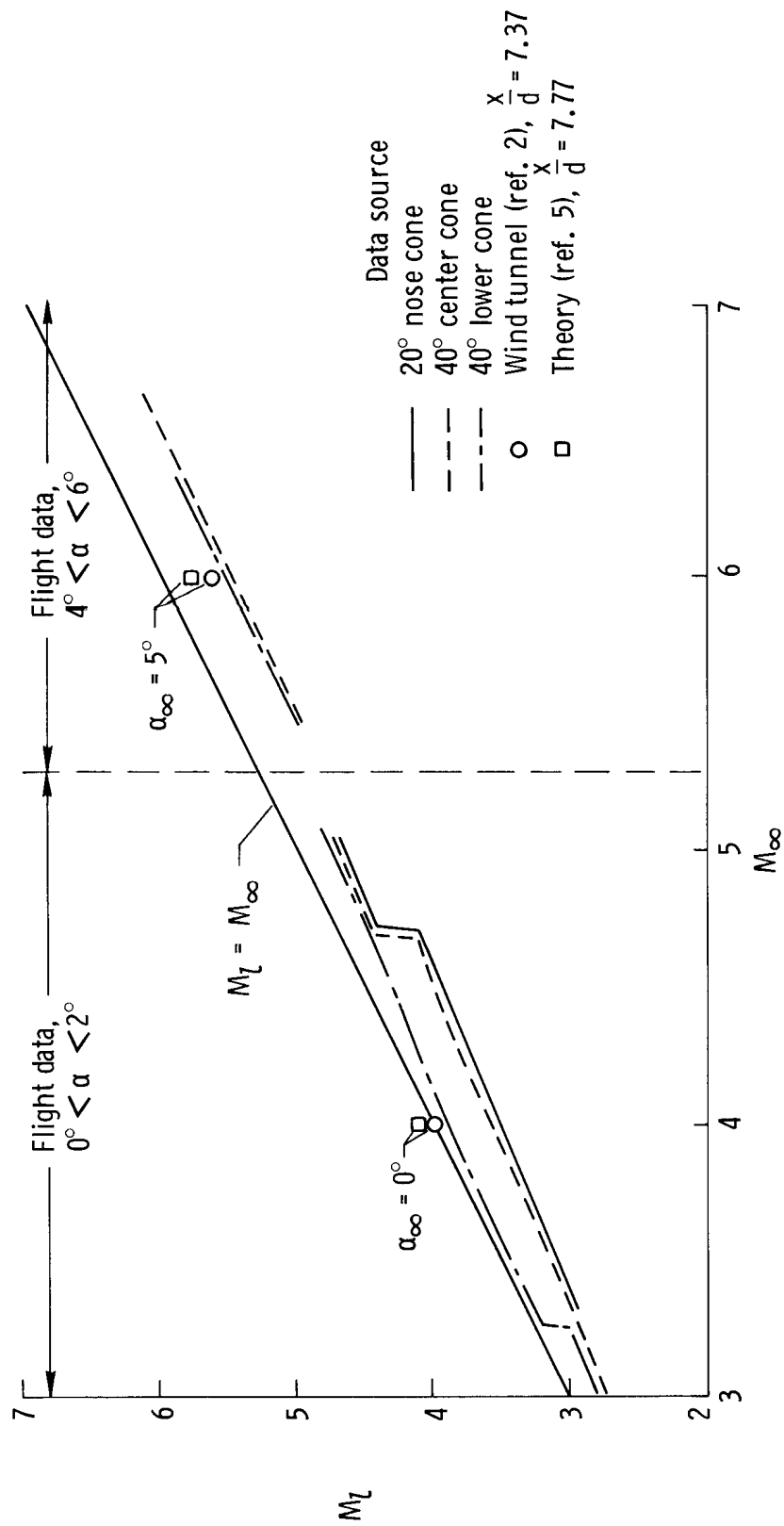


Figure 27. — Comparison of local Mach number at the ramjet spike tip from flight, wind tunnel, and theoretical calculations.

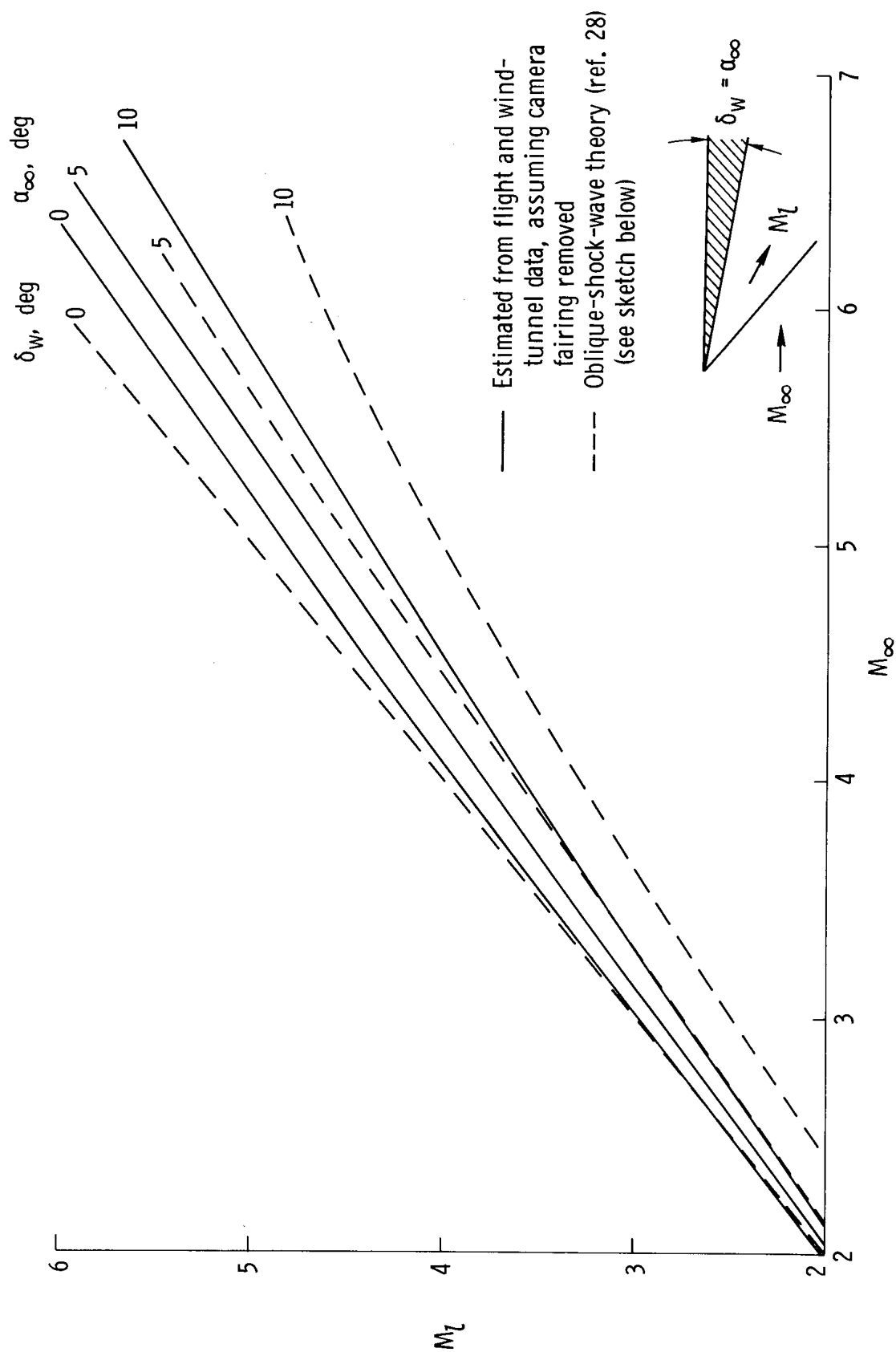


Figure 28. — Effect of M_∞ and α_∞ on estimated local Mach number at the ramjet spike tip assuming the camera fairing is removed.

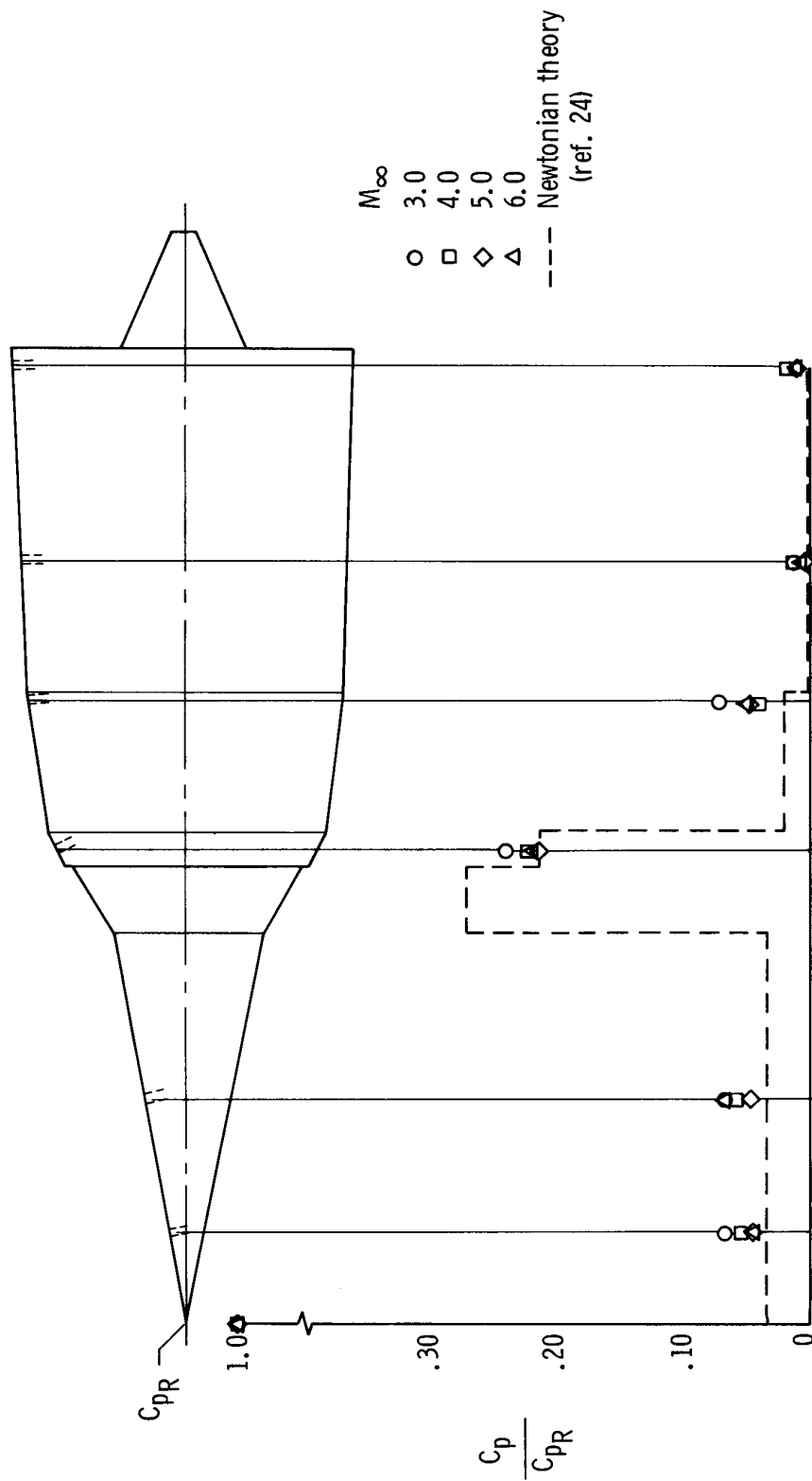


Figure 29. -- Ramjet-body surface static-pressure-coefficient ratios.
 α_∞ range 0° to 10° ; $\beta_\infty \approx 0^\circ$.